## ARTICLE

# Stromal and therapy-induced macrophage proliferation promotes PDAC progression and susceptibility to innate immunotherapy

Chong Zuo[1], John M. Baer[1], Brett L. Knolhoff[1], Jad I. Belle[1], Xiuting Liu[1], Angela Alarcon De La Lastra[1], Christina Fu[2], Graham D. Hogg[1], Natalie L. Kingston[1,3], Marcus A. Breden[1], Paarth B. Dodhiawala[1], Daniel Cui Zhou[1], Varintra E. Lander[1,3], C. Alston James[4,5], Li Ding[1,4], Kian-Huat Lim[1,4], Ryan C. Fields[4,5], William G. Hawkins[4,5], Jason D. Weber[1,6], Guoyan Zhao[6,7], and David G. DeNardo[1,3,4]

**Tumor-associated macrophages (TAMs) are abundant in pancreatic ductal adenocarcinomas (PDACs). While TAMs are known to proliferate in cancer tissues, the impact of this on macrophage phenotype and disease progression is poorly understood. We showed that in PDAC, proliferation of TAMs could be driven by colony stimulating factor-1 (CSF1) produced by cancer-associated fibroblasts. CSF1 induced high levels of p21 in macrophages, which regulated both TAM proliferation and phenotype. TAMs in human and mouse PDACs with high levels of p21 had more inflammatory and immunosuppressive phenotypes. p21 expression in TAMs was induced by both stromal interaction and/or chemotherapy treatment. Finally, by modeling p21 expression levels in TAMs, we found that p21-driven macrophage immunosuppression in vivo drove tumor progression. Serendipitously, the same p21-driven pathways that drive tumor progression also drove response to CD40 agonist. These data suggest that stromal or therapy-induced regulation of cell cycle machinery can regulate both macrophage-mediated immune suppression and susceptibility to innate immunotherapy.**

## Introduction

Macrophages are one of the most abundant immune cell types in the tumor microenvironment (TME; Noy and Pollard, 2014). Extensive studies have shown that macrophages can mediate tumor immunosuppression by both directly interacting with cytotoxic T cells and indirectly affecting T cell functions through secretions of immuno-modulators that create a favorable TME (DeNardo and Ruffell, 2019; Cassetta and Pollard, 2018; Doedens et al., 2010). Aside from their immunosuppressive phenotypes, macrophages are known to promote tumor initiation, angiogenesis, local invasion, and metastatic spread (Ruffell and Coussens, 2015; Hao et al., 2012; Cassetta and Pollard, 2018). Unsurprisingly, the presence of macrophages is found to be associated with a poor clinical outcome in many cancers, including pancreatic cancer (Cassetta and Pollard, 2018; Ino et al., 2013). As such, preclinical and clinical studies have focused on targeting tumor-associated macrophages (TAMs). These approaches, often consisting of macrophage-depleting strategies, have yet to show clinical success, in spite of showing efficacies in preclinical models (DeNardo and Ruffell, 2019; Cannarile et al., 2017; Poh and Ernst, 2018; Xiang et al., 2021). This suggests more studies are needed to understand the varied subset of macrophages in tumors and how they impact tumor immunity and cancer progression.

During tissue damage, macrophage numbers can be increased by multiple mechanisms. These include the expansion of tissue resident macrophage populations by local proliferation or new macrophages can be recruited from blood monocytes (Ginhoux and Guilliams, 2016). This balance is likely regulated by both the tissues and types of damage. In pancreatic ductal adenocarcinoma (PDAC), macrophages are derived from both monocyte and tissue-resident sources (Zhu et al., 2017). One consistent characteristic of TAMs from both sources in PDAC mouse models is that they are highly proliferative (Zhu et al., 2017). Notably, proliferation of macrophages is not only observed in tumors but also in injured and inflamed tissues (Hashimoto et al., 2013; Davies et al., 2011; Van Gassen et al.,

.............................................................................................................................................................................................................
[1]Department of Medicine, Washington University School of Medicine, St. Louis, MO, USA; [2]Department of Biology, Grinnell College, Grinnell, IA, USA; [3]Department of Pathology and Immunology, Washington University School of Medicine, St. Louis, MO, USA; [4]Siteman Cancer Center, Washington University School of Medicine, St. Louis, MO, USA; [5]Department of Surgery, Washington University School of Medicine, St. Louis, MO, USA; [6]Department of Cell Biology and Physiology, Washington University School of Medicine, St. Louis, MO, USA; [7]Department of Neuroscience, Washington University School of Medicine, St. Louis, MO, USA.

Correspondence to David G. DeNardo: ddenardo@wustl.edu.

Check for updates

2015). Under these conditions, inhibiting macrophage proliferation dramatically reduced macrophage number and inflammation (Tang et al., 2015). These observations raised the possibility that inhibiting macrophage proliferation in PDAC might limit the number of tumor-promoting macrophages.

Macrophage proliferative status is commonly associated with underlying macrophage phenotypes. IFN-γ and LPS inhibit macrophage proliferation and induce production of nitric oxide and inflammatory cytokines (Müller et al., 2017; Xaus et al., 2000; Marchant et al., 1994). IL-4 promotes macrophage proliferation and drives them to a $T_H2$-like phenotype (Jenkins et al., 2013). These observations led to the question of whether the macrophage proliferation machinery plays a role in regulating macrophage phenotypes.

In this study, we aimed to understand how the PDAC microenvironment drove local macrophage proliferation and what the net outcome of this was on tumor immunity and progression. We discovered that while cancer-associated fibroblast (CAF)–induced macrophage proliferation was important for sustaining TAM number, induction of p21 in TAMs by stromal colony stimulating factor-1 (CSF1) resulted in immunosuppression and tumor progression.

## Results

### Tumor-infiltrating macrophages are highly proliferative in PDAC

To evaluate human PDAC infiltration by TAMs, we utilized multiplex immunohistochemistry (mpIHC) to stain for CD68+ macrophages and CK19+ tumor cells in human PDAC tissues and found that CD68+ TAMs were more frequent in PDAC tissues when compared to adjacent normal pancreas tissues (Fig. 1 A). To further study infiltrating macrophages, we utilized a p48−Cre+/LSL-Kras$^{G12D}$/p53$^{flox/flox}$ (KPC) genetically engineered mouse model (GEMM), which spontaneously develops PDAC tumors and recapitulates the pathological features of human PDAC (Hingorani et al., 2003; Hingorani et al., 2005). As in human PDAC, we found that the number of F4/80+ TAMs increased paralleling disease progression (Fig. 1, B and C). Our previous studies have shown that these PDAC-infiltrating TAMs were sustained by both local proliferation and monocyte recruitment in animal models (Zhu et al., 2017). However, these studies did not assess the potential impact macrophage proliferation might have on tumor progression or tumor immunity.

To further investigate the significance and mechanisms of local proliferation of TAMs, we more deeply studied pancreatic tissues from GEMMs and human PDAC patients. We first evaluated the frequency of proliferating macrophages in human PDAC tumors by mass cytometry time of flight (CyTOF). Distinguishing major leukocyte populations based on surface markers, we found that CD68+CD64+ macrophages composed >15% of all infiltrating leukocytes (Fig. 1, D and E; and Fig. S1 A). Notably, these macrophages expressed high levels of the proliferation markers PCNA and Ki67 (Fig. 1 D). Ki67+ macrophages made up 20% of total macrophages, and this percentage was significantly higher than that of other leukocyte populations, such as neutrophils (Fig. 1 F and Fig. S1, B and C).

Next, we examined proliferating macrophages in tumors from KPC GEMMs. We observed >10% of F4/80+ cells were also Ki67$^{High}$ by mpIHC analysis (Fig. 1, G and H). The number and proliferation of TAMs were comparable in both p53$^{flox/+}$ and p53$^{R127H/+}$ orthotopic models (Fig. 1, I and J; and Fig. S1 D). In addition, we generated and analyzed single-cell RNA-sequencing (scRNAseq) data from normal pancreas, pancreatic tissues from KPC GEMMs, orthotopic PDAC tumors, and previously published human PDAC datasets (Peng et al., 2019; Fig. S1 E). In human PDACs, we found populations carrying both myeloid and proliferating signatures (Fig. 1, K and L). Similarly, in mouse datasets, we identified TAMs independent of cell cycle genes (Fig. S1 F); then, upon reclustering, we easily identified discrete clusters with cell cycle gene signatures (Fig. 1 M and Fig. S1 G). As expected, this cluster was expanded in PDACs compared to normal tissues (Fig. 1 N). Taken together, these data suggest that a significant portion of macrophages are actively proliferating in both murine and human PDAC tissues.

### CAFs drive macrophage proliferation through CSF1

To identify the cellular players that drove macrophage proliferation in PDAC, we investigated the cellular composition in the PDAC TME. As others have shown, PDAC tumors contain dense fibrotic stroma (Elyada et al., 2019; Schnittert et al., 2019; Waghray et al., 2013). mpIHC staining of PDAC tissues from KPC GEMMs revealed abundant PDPN+ CAFs surrounding CK19+ tumor cells (Fig. 2 A and Fig. S2 J). We next performed proximity analysis and found that TAMs were within 100 μm to both tumor cells and CAFs, but more frequently closer to PDPN+ CAFs than CK19+ tumor cells (Fig. 2 B). To test whether CAFs and tumor cells drove macrophage proliferation, we co-cultured bone marrow–derived macrophages (BMDMs) with either PDAC cell lines from KPC GEMMs or primary pancreatic fibroblasts. We found that PDAC cells and fibroblasts both led to increases in macrophage proliferation, as measured by BrdU incorporation. However, fibroblasts induced significantly higher levels of proliferation and increases in the number of macrophages (Fig. 2 C). Additionally, macrophage proliferation was not further enhanced by triple culture of PDAC cells and fibroblasts, suggesting the effects were not additive (Fig. 2 C, gray bars). To determine whether fibroblasts induced macrophage proliferation in a cell contact–dependent manner or through secreted factors, we repeated these assays in a transwell system. We found that without direct contact to BMDMs, fibroblasts still drove macrophage proliferation at almost a comparable level as the strong mitogen, CSF1 (Fig. 2 D).

To identify the relevant secreted factors from fibroblasts that drove macrophage proliferation, we profiled 111 soluble factors derived from KP-1, KP-2, or fibroblast-conditioned media and found that fibroblasts secreted significantly higher levels of CSF1 (Fig. 2 E). We measured the levels of CSF1 secreted by fibroblasts and three different PDAC cell lines (KP-1, KP-2, and KI) through ELISAs and confirmed that only fibroblasts produced high levels of CSF1 (Fig. 2 F). Next, we sought to determine whether CSF1 was necessary and sufficient for fibroblasts to drive macrophage proliferation. Both the addition of neutralizing αCSF1 IgG to the co-culture of BMDMs and fibroblasts and knocking-down CSF1
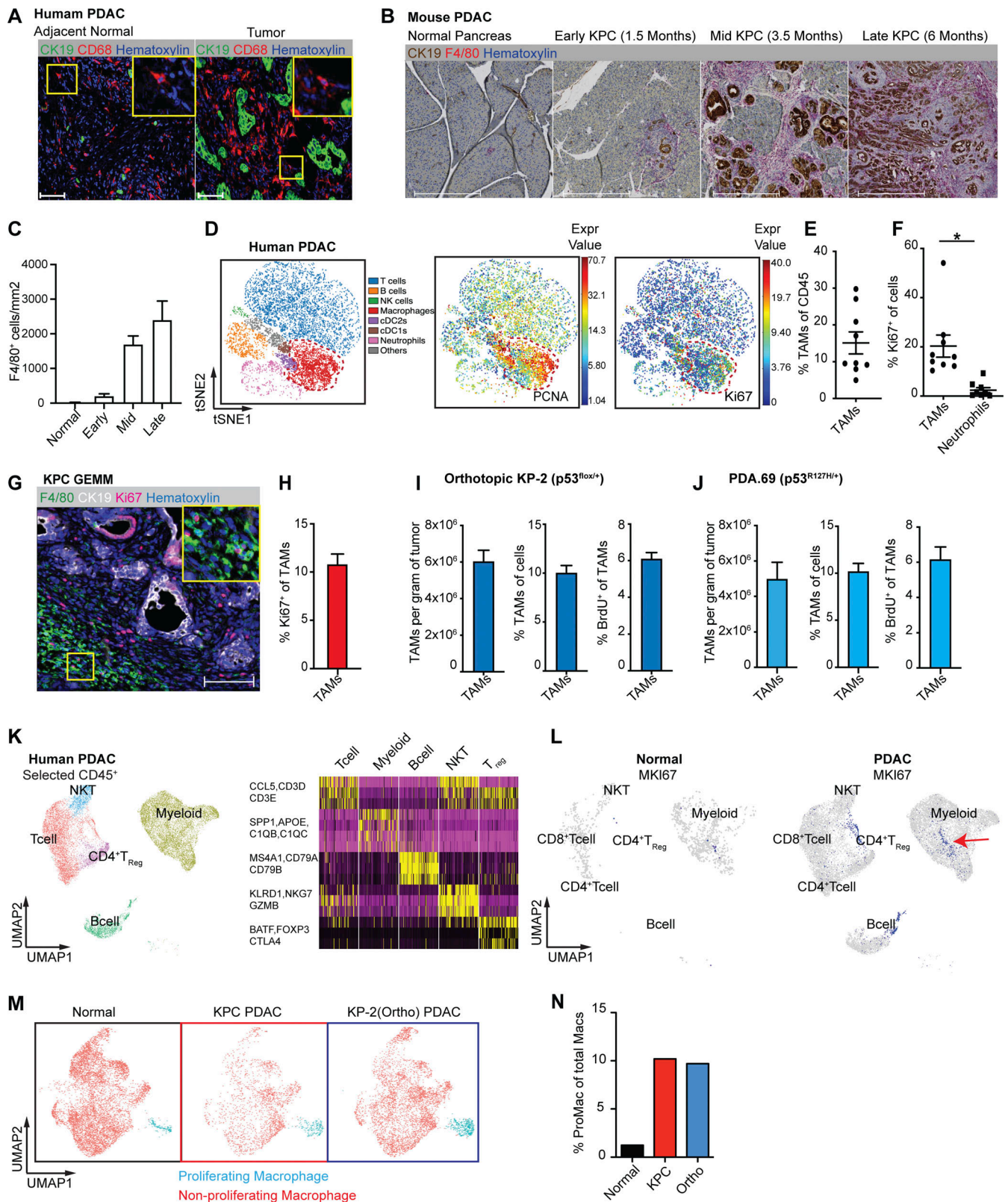
Figure 1. **PDAC-infiltrating macrophages are highly proliferative. (A)** Representative immunohistochemistry (IHC) analyses of CD68^{+} macrophages and CK19^{+} tumor cells in the late stage of PDAC tissues and adjacent normal tissues from human patients. Scale bars, 100 μm. **(B)** Representative IHC analyses of F4/80[+] macrophage and CK19^{+} tumor cells in normal pancreas, pancreatic tissues from early, mid, and late stages of KPC GEMMs. Scale bars, 500 μm. **(C)** Quantification of F4/80^{+} cells per millimeter of measured tissue area in B; n = 6–8 mice/group, two independent experiments. **(D)** Representative t-SNE plots of total normalized CD45^{+} cells from a PDAC patient, annotated with manually assigned cell identity. The macrophage cluster was marked with a red circle, and expressions of PCNA and Ki67 were explicitly displayed. **(E and F)** Dot plot displaying quantification of TAMs, Ki67^{+} TAMs, and Ki67^{+} neutrophils

across nine human PDAC patients. **(G and H)** Representative mpIHC displaying F4/80⁺ macrophages, CK19⁺ tumor cells, and Ki67⁺ proliferating cells in tumors from KPC GEMMs with quantification of Ki67⁺ macrophages; n = 6 mice, two independent experiments. Scale bars, 100 μm. **(I and J)** Quantification of total TAMs as per gram of tumor and percentage of cells, and BrdU incorporation of TAMs in orthotopic tumors from two PDAC cell lines. n = 6–8 mice. Data were consistent in at least four independent repeats for KP-2 and two independent repeats for PDA.69. **(K)** UMAP of realigned and reprocessed publicly available human PDAC dataset (Peng et al., 2019), displaying major CD45⁺ clusters and a heat map showing key gene expressions for each cluster. n = 21 PDAC samples, n = 6 normal samples. **(L)** UMAP plots displaying normalized expression levels of MKI67 across subpopulations with red arrow pointing to MKI67 expressing myeloid cells. **(M and N)** UMAP displaying proliferating macrophages and non-proliferating macrophage clusters across the mouse scRNAseq dataset with quantification in N. Data are presented as the mean ± SEM. *, P < 0.05. For comparisons between any two groups, Student's two-tailed t test was used.

---

in fibroblasts by siRNA in transwell assays resulted in a loss of fibroblast-driven macrophage proliferation and number expansion (Fig. 2, G–I). These data suggest that CSF1 secreted from fibroblasts is both necessary and sufficient to macrophage proliferation in vitro.

To confirm CAFs drive TAMs proliferation in in vivo pancreatic tissue, we analyzed scRNAseq datasets from both mouse and human. In a previously published dataset (Hosein et al., 2019) of pancreatic tumors from three PDAC GEMMs, including *Kras^{LSL-G12D/+}Ink4a^{fl/fl}Ptf1a^{Cre/+}* (KIC), *Kras^{LSL-G12D/+}Trp53^{LSL-R172H/+}Ptf1a^{Cre/+}* (KP^{R172H/+}C), and *Kras^{LSL-G12D/+}Trp53^{fl/fl}Pdx1^{Cre/+}* (KPfC), we found that fibroblasts expressed higher levels of CSF1 than other cell types (Fig. 3, A and B). In a human PDAC dataset (Peng et al., 2019) comprised of 21 PDAC samples, fibroblasts also expressed a higher level of CSF1 than tumor cells and other cells within the TME (Fig. 3, C and D). Others have also detected CSF1 in the cultures of primary CAFs from PDAC patients (Samain et al., 2021). Collectively, these data suggest that fibroblasts are the main producers of CSF1 in the PDAC TME. Next, we injected αCSF1 IgG into mice bearing orthotopic KP-2 tumors and measured macrophage proliferations 12 and 24 h after the injection. Similar to the in vitro experiments, we found a significant reduction in the percentage of macrophages undergoing proliferation, measured by BrdU incorporation (Fig. 3, E and F). We have previously shown that sustained CSF1 depletion, exceeding 48 h, led to macrophage depletion by apoptosis (Zhu et al., 2014). However, in this short period of treatment time, we did not observe significant change in macrophage number (Fig. 3 G). Additionally, we found that proliferation of monocytes was minimal and not significantly affected by αCSF1 IgG treatment (Fig. 3 H), confirming that the reduction of proliferation was mainly from macrophages. Taken together, these data suggest that CSF1 secreted by CAFs drives local macrophage proliferation in pancreatic cancer.

### The p21 cell cycle–dependent kinase inhibitor was induced in TAMs by CAF-derived CSF1

We next asked whether the macrophage proliferation machinery regulated by CAF-derived CSF1 could impact the TAM phenotype. We first examined the expressions of several critical cell cycle regulators in BMDMs following treatment with either CSF1, the proliferative mitogen, or LPS, which is known to blunt macrophage proliferation (Liu et al., 2016; Fig. S2 A). We found that when BMDMs were treated with CSF1, overall protein levels of c-Myc and cyclin D1 were upregulated while p27^{Kip1} was reduced (Fig. 4 A). BMDMs treated with LPS showed the opposite result. These changes are consistent with the existing roles of cell cycle promoters (c-Myc and cyclin D1) and a cell cycle

inhibitor (p27^{Kip1}; Liu et al., 2016; Matsushime et al., 1991). However, surprisingly, we found p21^{Waf/Cip1}, a cell cycle inhibitor (Cazzalini et al., 2010; Dutto et al., 2015; Brugarolas et al., 1999), was strongly induced by both CSF1 and CAF co-culturing (Fig. 4, B and D). To further investigate this p21 induction, we performed a kinetic study of p21 expression in BMDMs and found that the p21 protein was induced by CSF1 within 6–12 h, which was prior to S phase entry at 24–48 h after CSF1 administration, as measured by BrdU (Fig. 4, B and C). Similar kinetics and cell cycle transit were found when BMDMs were cultured with fibroblasts in a transwell assay (Fig. 4, D and E). Adding αCSF1-neutralizing antibody into transwell assay returned expression of p21 in BMDMs to baseline condition (Fig. S2 M). These data suggest that fibroblast-derived CSF1 induced p21 expression and could impact both macrophage cell cycle and phenotype.

To test whether p21 induction impacted macrophage phenotype, we knocked down p21 expression in BMDMs by siRNA in the presence of CSF1. We found that p21 knockdown resulted in a significant increase in the percentage of macrophages that entered S phase, confirming p21's inhibitory role in the G1/S transition (Fig. S2, B and C). To assess macrophage phenotypic changes after p21 knockdown, we performed gene profiling analysis followed by RT-qPCR validation of altered gene expressions. Transcription profiling revealed >300 genes that were differentially expressed in BMDMs upon p21 knockdown in the presence of tumor conditioned medium (Fig. 4 F). Over-representation analysis of differentially expressed genes (DEGs) demonstrated that p21 knockdown in BMDMs resulted in the upregulation of genes involved in cell cycle progression, as expected, but also unexpectedly, it upregulated IFN-α and -γ responses (Fig. 4 G). RT-qPCR validation also found upregulation of IFN-related genes, *IFIT3*, *CD40*, *IFN-α*, and *IFN-β*. Notably, gene expression of cyclins involved in the early cell cycle (G1), including *CCND1* and *CCNE*, were unchanged, while *CCNA*, an S phase cyclin, was upregulated (Fig. 4 H). Together, these data suggest that in addition to its canonical role in regulating S phase entry, p21 might suppress IFN-signaling pathways. In a CSF1-rich TME like PDAC, elevated p21 expression in macrophages might play a prominent role in impairing tumor immunity (Hervas-Stubbs et al., 2011).

Based on the significant presence of CSF1-producing CAFs in the PDAC TME, we hypothesized that p21 might be chronically high in TAMs and thus might drive their immune-suppressive phenotype. We first evaluated p21 expression in human PDAC tumors by CyTOF and found PDAC TAMs frequently expressed high levels of p21 (Fig. 4 I and Fig. S2 D). Similarly, KPC tumors also had significant numbers of F4/80⁺ TAMs expressing high
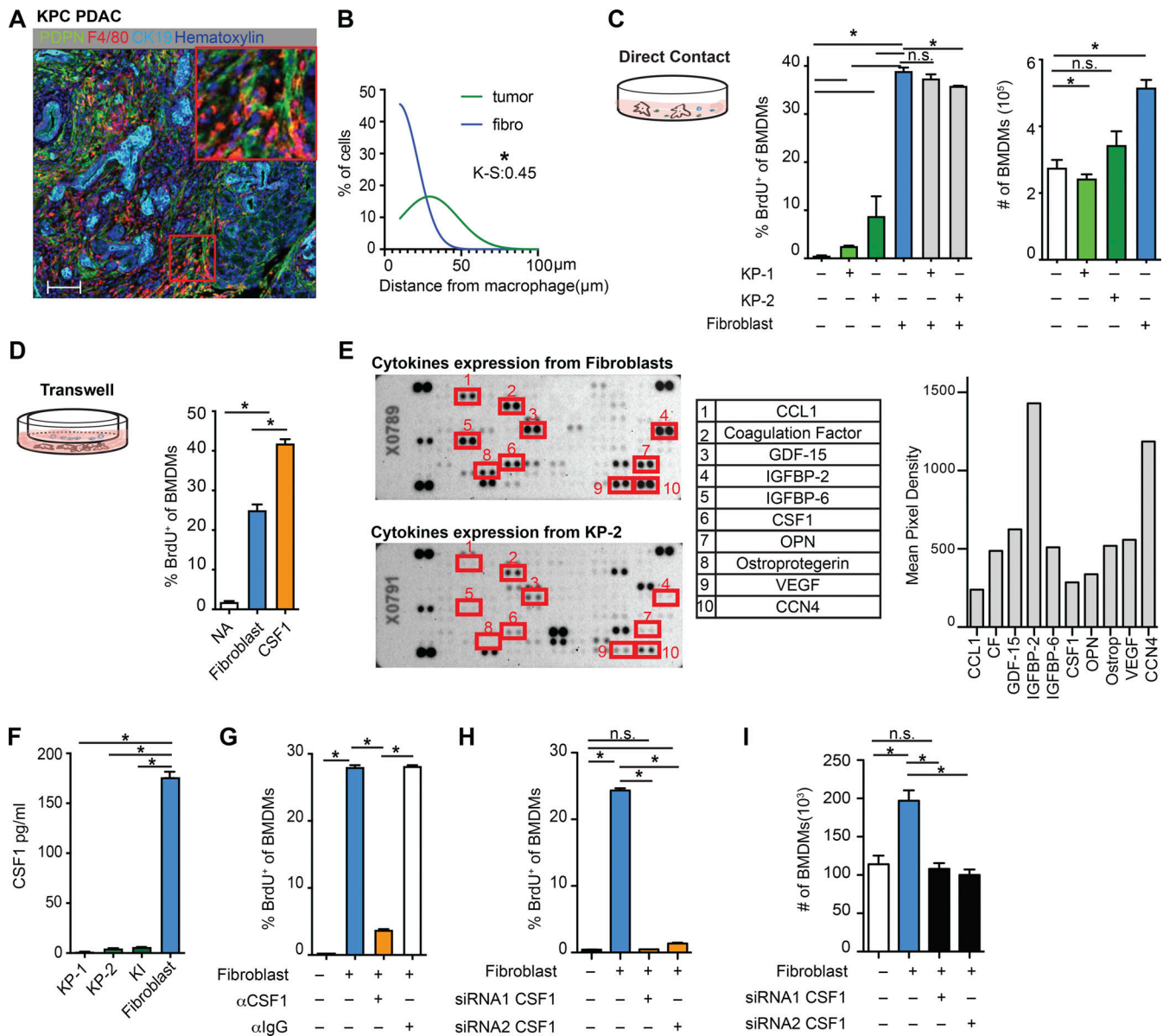
**Figure 2. Fibroblasts drive macrophage proliferation through CSF1. (A)** Representative mpIHC image of KPC mouse PDACs displaying αSMA+ (white) fibroblasts, CK19+ (teal) tumor cells, and F4/80+ (green) macrophages. Scale bars, 100 μm. **(B)** Frequency distribution of Pdpn+ fibroblasts (blue curve) and CK19+ tumor cells (green curve) to a nearest F4/80+ macrophage. $n$ = 6 KPC mice. **(C)** The BrdU incorporation and number of BMDMs in co-culture with KP-1, KP-2, fibroblasts, or the combination for 48 h, BrdU pulsed for the last 6 h; $n$ = 6. **(D)** The BrdU incorporation of BMDMs when cultured with fibroblasts in a transwell assay or 10 ng/ml of CSF1 for 48 h, and BrdU pulsed for the last 6 h; $n$ = 3. **(E)** Representative image of a cytokine antibody array resulting from fibroblast- and KP-2–conditioned media, highlighting the top 10 highly expressed cytokines in fibroblast-conditioned medium and the corresponding mean pixel densities. The arrays were repeated two times. **(F)** Bar graph shows the concentrations of CSF1 from three tumor-conditioned media (KP-1, KP-2, and KI) and fibroblast-conditioned medium measured by an ELISA. **(G)** BrdU incorporation of BMDMs in co-culture with fibroblasts treated with 2 μg of aCSF1 or 2 μg of aIgG for 24 h, and BrdU pulsed for the last 6 h; $n$ = 3. **(H and I)** BrdU incorporation and number of BMDMs in transwell cultures with fibroblasts with or without siRNA knockdown for CSF1; $n$ = 3. Data are presented as the mean ± SEM. *, $P < 0.05$. All in vitro assay data are representative of two to three agreeing independent repeats. For comparisons between any two groups, Student's two-tailed $t$ test was used. Frequency distributions were compared using the nonparametric Kolmogorov–Smirnov test.

levels of p21 evaluated by mpIHC (Fig. S2 E). Finally, scRNAseq analyses suggested that TAMs from both human and murine PDAC tissues had higher levels of p21 gene expressions than macrophages in normal tissues (Fig. 4 J and Fig. S2 F). The elevation of p21 in PDAC tumors could be a result of increased number of macrophages entering cell cycle as shown in Fig. 1, M and N. However, we observed that in CyTOF, TAMs that were high in p21 expression were not necessarily high in the expression of PCNA or Ki67 (Fig. 4 I and Fig. 1 D), suggesting p21 expression was not only up in proliferating TAMs. In addition, we did not find a significant difference in the p21 protein levels between Ki67+ vs. Ki67− TAMs by CyTOF, nor did we find significant difference in p21 gene expression in proliferating and non-proliferating clusters of TAMs in scRNAseq data (Fig. S2, G and H). Collectively, these
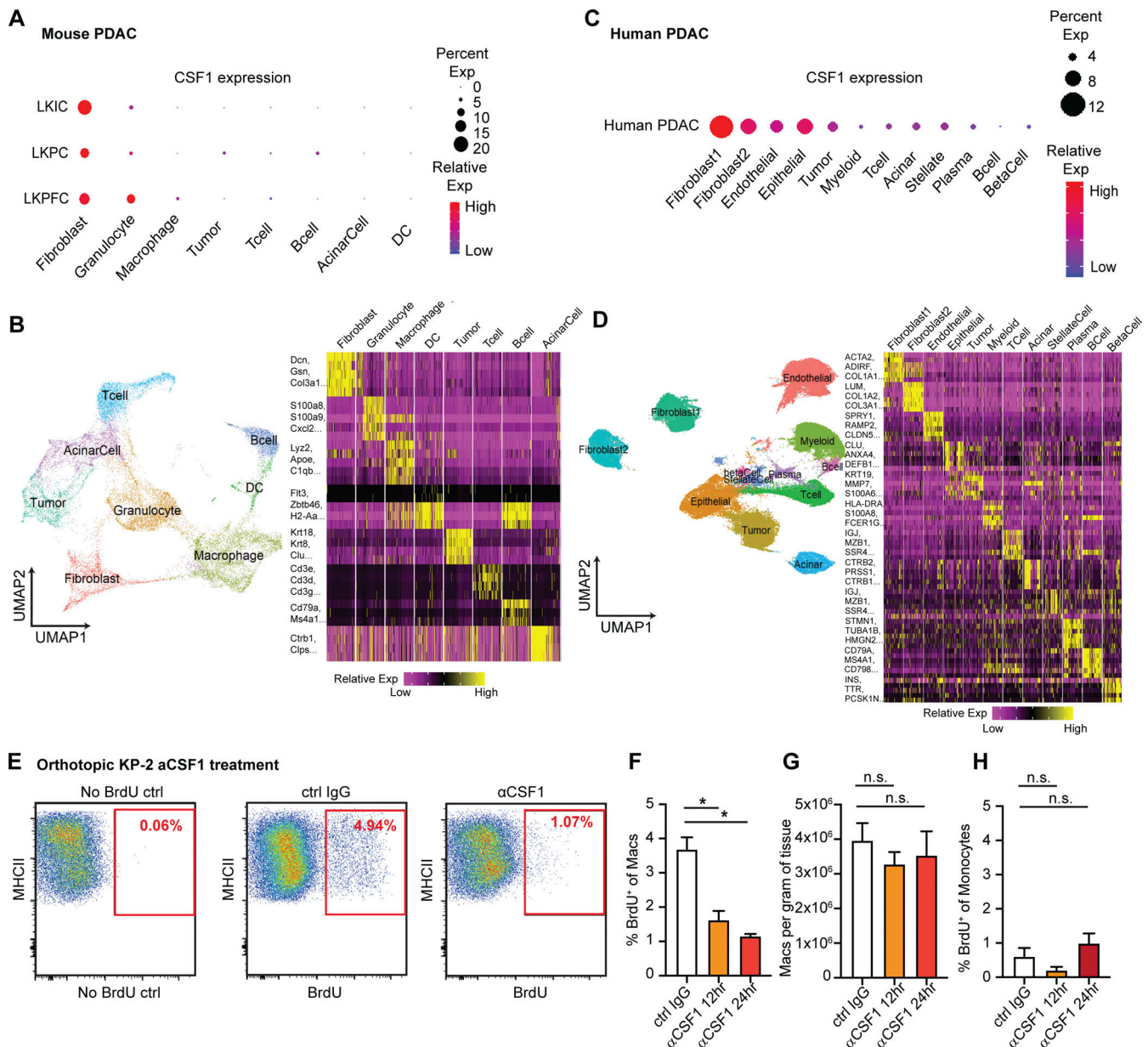
Figure 3. **CAFs drive tumor associated macrophage proliferation through CSF1. (A)** Dot plot summarizing CSF1 expressions in different cell types across three mouse PDAC models from the publicly available scRNAseq dataset (Hosein et al., 2019). **(B)** UMAP dimensionality reduction plot of integrated cells from LKIC, LKP $^{R172H/+}$C, and LKPFC GEMMs in scRNAseq dataset used in A, annotated with different cell types. Data were filtered and reprocessed as described in the Materials and methods. **(C)** Dot plot displaying CSF1 expressions in different cell types across 21 human PDAC patient samples from the publicly available scRNAseq dataset (Peng et al., 2019). **(D)** UMAP dimensionality reduction plot of integrated cells from 21 pancreatic adenocarcinoma patients used in C, annotated with different cell types. **(E–H)** Representative flow cytometry plot and quantification bar plot showing BrdU+ macrophages and monocytes, and total number of macrophages following αIgG control or αCSF1 injections; n = 6–8 mice per group. Data are presented as the mean ± SEM. *, P < 0.05. For comparisons between any two groups, Student's two-tailed t test was used.

results suggest that elevated p21 expression in PDAC TAMs is unlikely to be solely caused by cell cycle entry/progression; it may become elevated by other factors in the TME and regulate TAMs phenotype.

To further assess the potential phenotypic differences in TAMs based on p21 expression, we generated and analyzed data from four scRNAseq datasets, including one from human (Peng et al., 2019) and three from PDAC mouse models (Hosein et al., 2019). We identified macrophage populations in each mouse

dataset and myeloid populations in human dataset based on known macrophage markers after unsupervised clustering and UMAP projection (Fig. S1 F and Fig. 3, B and D). We then stratified macrophages (myeloid cells in human) based on p21 gene expressions to the p21$^{High}$ and p21$^{Low}$ grouped in each dataset (Fig. 4 K). Notably, UMAP dimension reduction revealed the similar spatial distributions of p21$^{High}$ and p21$^{Low}$ macrophages in tumors from mouse GEMM and orthotopic models, suggesting shared characteristics among the same group of
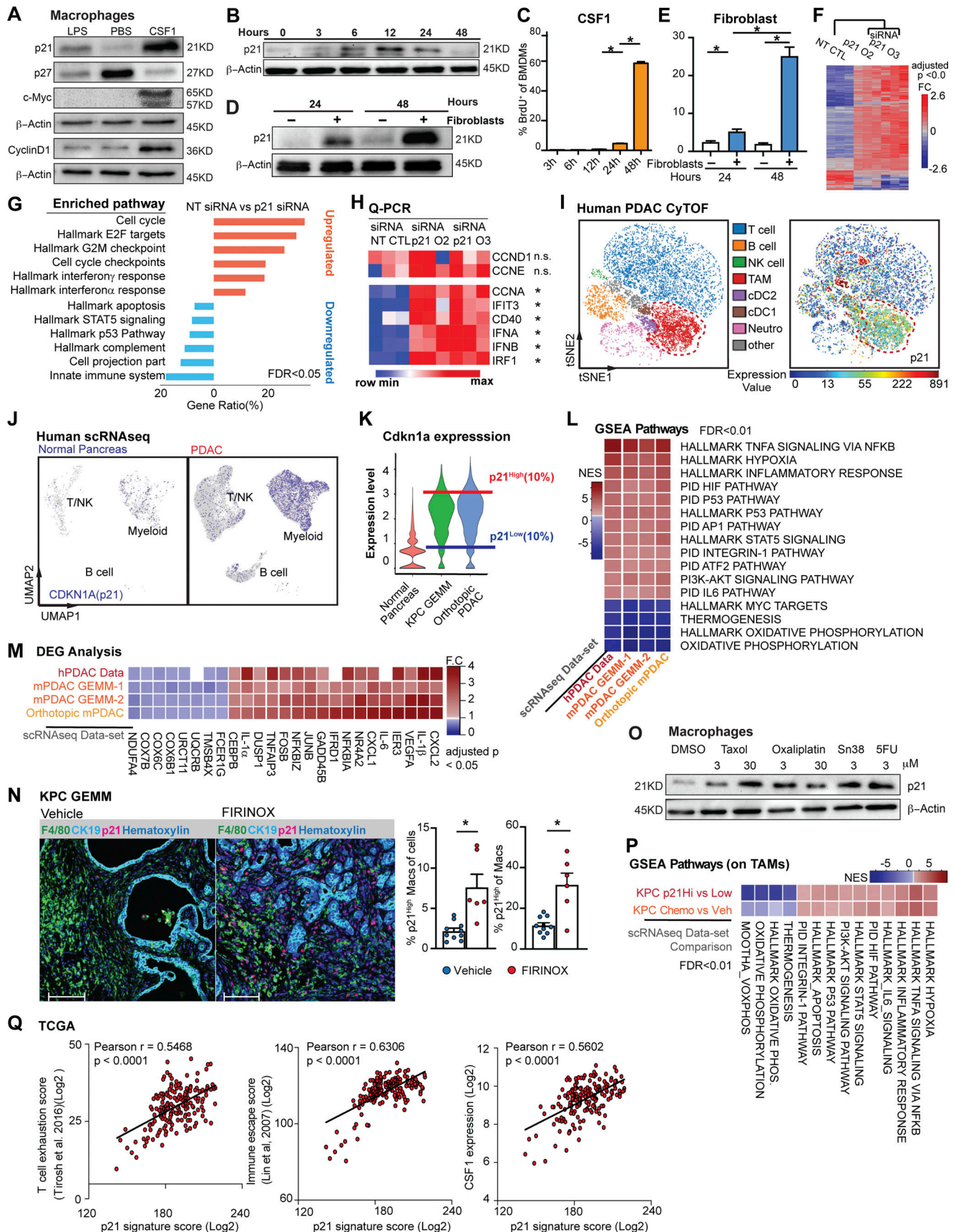
**Figure 4. The p21 cell cycle–dependent kinase inhibitor is induced by CSF1 and regulates the macrophage phenotype. (A)** Immunoblots of p21, p27, c-Myc, and cyclinD1 in BMDMs after treatment with 100 ng/ml of LPS or CSF1 for 24 h. The experiments were repeated three times. **(B and C)** Immunoblot

displaying p21 expression in BMDMs following 4 ng/ml CSF1 treatment at time 0 with quantification of BrdU⁺ BMDMs shown in C. BrdU was added at time 0 and pulsed until harvest. BMDMs were starved without CSF1 overnight. **(D)** Immunoblot displaying p21 expression in BMDMs combined with fibroblasts in transwell assays at time 0. BMDMs were starved without CSF1 overnight. **(E)** Bar plot displaying the quantification of BrdU⁺ BMDMs in a transwell assay, as in D. **(F)** Heat map displaying the microarray analysis of DEGs between non-target siRNA–treated or siRNA targeting for p21–treated BMDMs cultured in tumor-conditioned medium for 24 h; n = 3 per group. Genes were filtered with adjusted P < 0.05 and fold-change > or <1.5. **(G)** Bar graph displaying top over-representation analysis of DEGs in F to known biological functions (GO, KEGG, Reactome, and MSigDB) with an FDR < 0.05. **(H)** Heat map displaying qPCR analysis of gene expressions of cell cycle and IFN-related genes between non-target siRNA–treated or siRNA targeting for p21–treated BMDMs cultured in tumor-conditioned medium for 24 h; fold-change >1.5, n = 3/group of the comparison. **(I)** Representative t-SNE plot displaying major cell types from CyTOF analysis of a human PDAC patient (same as in Fig. 1 D) with macrophages circled in red and p21 expression. **(J)** UMAP displaying *CDKN1A* gene expression in CD45⁺ cells from the human PDAC scRNAseq dataset (Peng et al., 2019) with annotation of key cell types. **(K)** Violin plot showing the expression levels for p21 gene in macrophage clusters from integrated scRNAseq analyses of the mouse normal pancreas and pancreatic tissue from KPC GEMMs and orthotopic KP-2 tumor-bearing mice. Representative lines were drawn for two groups of stratified macrophages based on the top 10% of p21 expression and bottom 10% of p21 expression. **(L)** Heat map of net enrichment score (NES) of shared enriched pathways identified by GSEA analysis comparing the two groups of macrophages (p21^High vs. p21^Low) in human PDAC scRNAseq dataset (Peng et al., 2019), KPC GEMMs (Hosein et al., 2019) and orthotopic scRNAseq data. Enriched pathways were selected by FDR < 0.01. **(M)** Heat map displaying the shared DEGs when comparing p21^High to p21^Low TAMs in each dataset with adjusted P < 0.05 and fold-change >1.2 or <0.8. p21^High signature score was created utilizing filtered DEGs with fold-change >1.5 across three mouse scRNAseq datasets. **(N)** Representative mpIHC image displaying F4/80⁺ TAMs, CK19⁺ tumor cells, and p21⁺ cells in KPC GEMM treated with dimethyl sulfoxide or FIRINOX (i.v; 50 mg/kg 5-FU, 25 mg/kg irinotecan, 6.6 mg/kg oxaliplatin) for 24 h with quantification of p21⁺ TAMs as total cells and total TAMs on the right. Scale bars, 100 μm. **(O)** Immunoblots showing expressions of p21 in wild-type BMDMs after chemotherapeutics treatment for 24 h. **(P)** Heat map of NES of shared enriched pathways identified by GSEA analysis in comparing p21^High to p21^Low TAMs in KPC GEMM PDAC and in comparing chemotherapeutic-treated KPC GEMM PDAC to DMSO-treated KPC GEMM PDAC with FDR < 0.05. **(Q)** Correlation plots with Pearson coefficients (r) of p21 signature score vs. T cell exhaustion score (Tirosh et al., 2016), immune escape score (Lin et al., 2007), and CSF1 expression from TCGA PDAC PanCancer Atlas study (n = 180). All graphs are expressed as the mean ± SEM. *, P < 0.05. All in vitro assays and immunoblots are representative of two to three agreeing independent repeats unless otherwise specified. For comparisons between any two groups, Student's two-tailed t-test was used, except for F and M where the Bonferroni correction was used and for L and P where the FDR was used. Source data are available for this figure: SourceData F4.

TAMs in different models (Fig. S2 I). To understand what these common phenotypes were, we performed gene set enrichment analysis (GSEA) between p21^High and p21^Low macrophages in each dataset. Across all four datasets and both species, we found that hallmarks typically associated with the TNF-α signaling pathway, hypoxia, and STAT5 signaling were upregulated in p21^High macrophages, while oxidative phosphorylation pathways were upregulated in p21^Low macrophages (p21^Low myeloid cells in human; Fig. 4 L). Although TNF-α and its signaling pathway are proinflammatory, prolonged and irregulated activation are frequently considered immunosuppressive in tumors. In this respect, TNF-α can mediate T cell exhaustion, CD8⁺ T cell death, and expansion of myeloid-derived suppressor cells and regulatory T cells (Tregs) to promote tumor progression and metastasis (Salomon et al., 2018; Balkwill, 2006). Consistent with the enrichment for TNF-α via the NF-κB signaling pathway, expressions of IL-1α, IL-1β, and NF-κB components were also upregulated in p21^High macrophages (Fig. 4 M). Together, these data suggest that TAMs with high p21 expression acquire an inflammatory but potentially immunosuppressive gene signature.

PDAC patients are frequently treated with cytotoxic chemotherapies that can impact both tumor cells as well as stromal cells. Therefore, we sought to next determine whether chemotherapy could impact TAM proliferation and p21 expression and thus influence TAM-immunosuppressive programs. First, we treated KPC GEMM with either a combination of 5-FU, irinotecan, and oxaliplatin or a combination of gemcitabine and paclitaxel (GEM/PTX). Both chemotherapies combinations are frontline treatments for pancreatic cancer patients. We analyzed p21^HighF4/80⁺ TAMs 24 h later by mpIHC and found that the number of p21^High TAMs significantly increased after both chemotherapy treatments (Fig. 4 N and Fig. S2 L). To determine whether this was a direct effect of chemotherapeutic

exposure, we treated BMDMs with four different chemotherapeutics for 24 h and observed similar inductions of p21 (Fig. 4 O). Finally, to assess whether induction of p21 might be correlated with changes in macrophage phenotype induced by chemotherapy, we analyzed TAMs from KPC GEMMs treated with vehicle or GEM/PTX by scRNAseq. We found striking similarity in the pathways enriched in TAMs from mice treated with GEM/PTX compared to vehicle and pathways found when we stratified TAMs in vehicle treatment mice by p21 expression (Fig. 4 P). Similarly, TAMs from GEM/PTX-treated KPC mice showed higher expression of the p21^High gene signature when compared to vehicle (Fig. S2 K). These data suggested that p21 was induced by both stromal interaction and chemotherapy treatments and correlated with inflammatory and likely immunosuppressive phenotypes in PDAC TAMs. Next, we analyzed the p21^High TAM signature in The Cancer Genome Atlas (TCGA) datasets and found strong correlation with signatures of "T cell exhaustion" (Tirosh et al., 2016) and "immune escape" (Lin et al., 2007; Fig. 4 Q). Additionally, the p21 signature strongly correlated with CSF1 expression (Fig. 4 Q). These data suggest that stromal CSF1–induced p21 expression in TAMs may drive dysfunctional T cell–mediated tumor control.

## Expression of p21 drove the tumor-promoting phenotype in macrophages

To better understand the impact of induction of p21 expression on the macrophage phenotype, and on the PDAC TME, we engineered a mouse designed to constitutively express p21 in myeloid cells. The construct contained the *p21* gene under the control of a CAG promoter and a lox-stop-lox case. Downstream of the *p21* gene, the construct also contained an internal ribosome entry site (IRES) and YFP gene for visualization. The construct was then integrated into the ROSA locus of pure C57/B6 mice (ROSA-CAG-LSL-p21-IRES-YFP, p21⁺/ʷᵗ; Fig. 5 A). Then,
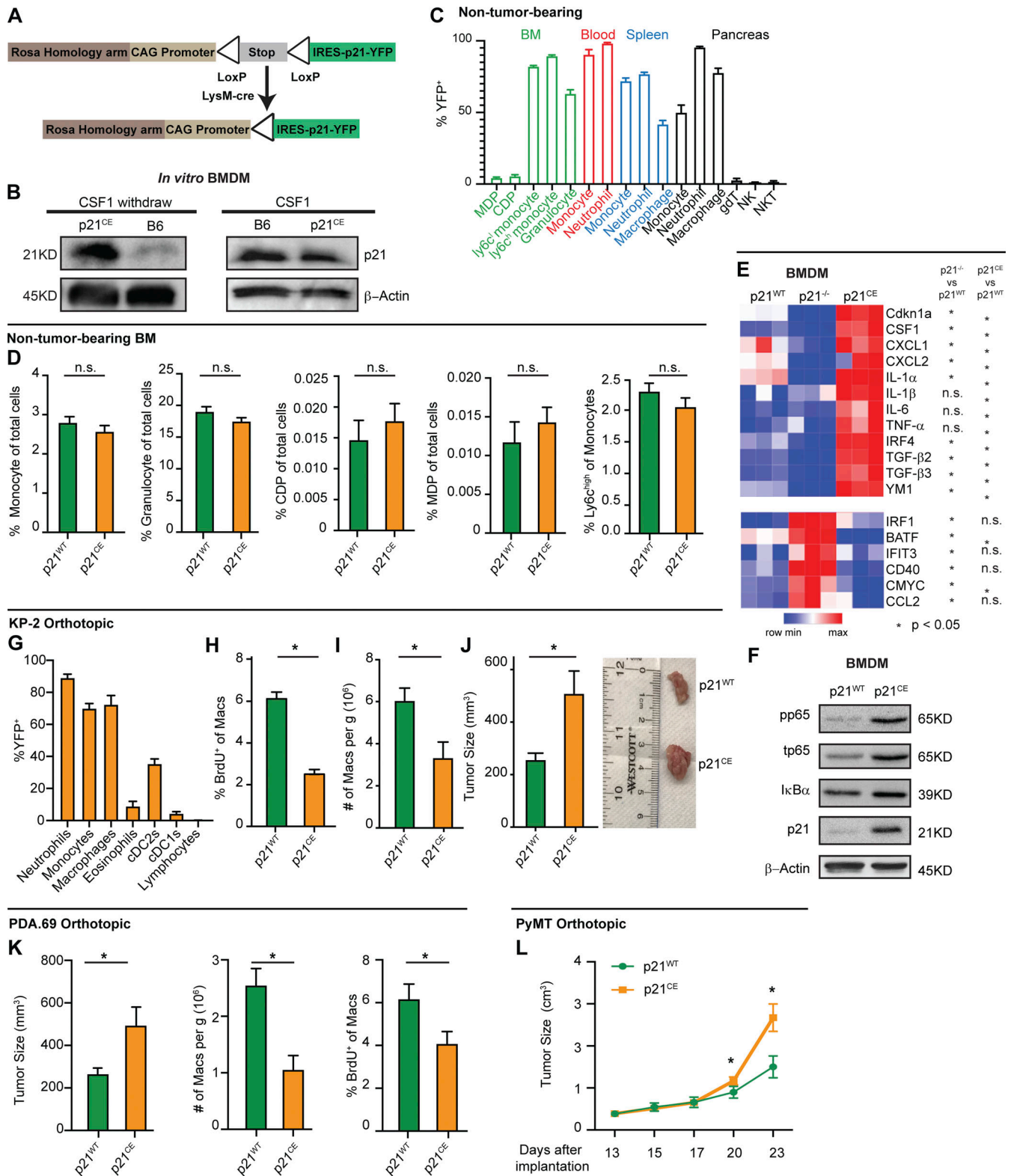
Figure 5. **Expression of p21 drives tumor-promoting phenotypes in macrophages.** **(A)** Genetic loci for the p21[CE] model. **(B)** Immunoblot for p21 expression in p21[CE] or B6-derived BMDMs with or without 10 ng/ml of CSF1 treatment for 24 h. Experiments were consistent in at least three independent repeats. **(C)** Bar plot displaying the percentage of YFP+ cells in non-tumor-bearing p21[CE] mice; n = 4. **(D)** Bar plot showing flow cytometry quantification of cellular composition in non-tumor-bearing bone marrow from p21[CE] and p21[WT] mice; n = 6–9 mice/group. Data were consistent in two independent repeats. **(E)** Heat map displaying gene expression analysis of BMDMs derived from non-tumor-bearing p21[WT], p21^{−/−}, and p21[CE] mice treated with 10 ng/ml of CSF1 for 24 h, by RT-qPCR; n = 3/group. Data was consistent from three independent repeats. **(F)** Immunoblots for phos-p65, total p65, IκB, and p21 expression in p21[CE] or p21[WT] BMDMs after withdrawing CSF1 overnight. Data were consistent in four independent repeats. **(G)** Flow cytometry quantification of YFP+ cells in p21[CE] mice

bearing orthotopic KP-2 tumors; $n = 6-7$ mice. **(H and I)** Quantification of BrdU⁺ macrophages and density of macrophages in tumors of p21$^{CE}$ and p21$^{WT}$ mice; $n = 6-7$ mice/group. Data were pooled across multiple independent experiments. **(J)** Bar plot displaying the tumor sizes in p21$^{CE}$ and p21$^{WT}$ mice, 21–27 d following orthotopic implantation of KP-2 tumor cells; $n = 8-10$ mice/group. Data were pooled from multiple independent experiments. **(K)** Bar plot displaying tumor sizes, density of macrophages, and quantification of BrdU⁺ macrophages from p21$^{CE}$ and p21$^{WT}$ mice, 21–23 d after the orthotopic implantation of the PDA.69 cell line; $n = 8-10$ mice/group. Data were pooled from multiple agreeing and independent experiments. **(L)** Caliper measurement of orthotopic PyMT in p21$^{WT}$ and p21$^{CE}$ mice; $n = 6-8$ mice/group. All graphs are expressed as the mean ± SEM. *, $P < 0.05$. All in vitro assays are representative of two to three agreeing independent repeats unless otherwise specified. For comparisons between any two groups, Student's two-tailed $t$ test was used. Source data are available for this figure: SourceData F5.

p21$^{+/wt}$ mice were crossed with LysMCre mice to induce p21 expression in myeloid cells. The resulting LysM$^{+/+}$/p21$^{+/wt}$ mice were termed "p21-constitutive expression" (p21$^{CE}$) mice.

To confirm that p21 expression was induced in macrophages from p21$^{CE}$ mice, we measured p21 protein levels in BMDMs from p21$^{CE}$ mice in the presence and absence of CSF1. We found BMDMs from p21$^{CE}$ mice expressed significantly higher levels of p21 protein in the absence of CSF1 compared to control BMDMs (Fig. 5 B). However, in the presence of CSF1, which strongly induced p21 expression in wild-type BMDMs (Fig. 4, A and B), both p21$^{CE}$ and p21$^{WT}$ BMDMs had similar p21 expressions. These data indicated that macrophages from the p21$^{CE}$ mouse model retained high p21 expression without stimuli and that the expression was at a physiological level comparable to CSF1 exposure or fibroblast co-cultures.

Given that LysMCre is known to be expressed in various myeloid compartments, including granulocytes and monocytes (Abram et al., 2014), we next examined whether the hematopoietic system was altered in p21$^{CE}$ mice. Flow cytometry analysis of non-tumor-bearing p21$^{CE}$ mice revealed that YFP, a surrogate for transgenic p21, was mainly expressed in mature monocytes, macrophages, and granulocytes/neutrophils in the blood, bone marrow, spleen, and pancreas, but minimally expressed in bone marrow progenitors and lymphocytes (Fig. 5 C). Corresponding to the lack of expression in progenitor cells, we did not find major changes in the cellular composition of bone marrow or blood in non-tumor-bearing p21$^{CE}$ mice compared with controls, as assessed by flow cytometry or by blood count analysis (Fig. 5 D and Fig. S3, A–C). Taken together, these data suggested that p21 was mainly expressed in mature myeloid cells in p21$^{CE}$ mice, but not in progenitors, and it did not greatly impact hematopoiesis.

As shown above in the scRNAseq data and gene-profiling analysis after p21 siRNA knockdown, p21 expression regulated the macrophage phenotype. To assess whether macrophages from p21$^{CE}$ mice had similar phenotypic changes, we profiled gene expressions of BMDMs from p21$^{WT}$, p21$^{CE}$, and p21$^{-/-}$ (Jax mice) mice in the presence of CSF1. We found that inflammatory cytokines/chemokines, *CXCL1*, *CXCL2*, *IL-1α*, *IL-1β*, *IL-6*, and *TNF-α* were upregulated in p21$^{CE}$ mice but reduced or not changed in p21$^{-/-}$ mice (Fig. 5 E). In addition, the IFN regulatory factor 4 (IRF4)–mediated macrophage alternative activated genes, *YM1* and *TGF-β*, were also upregulated. In contrast, p21$^{-/-}$ BMDMs had elevated levels of the IFN-related genes, *IRF1*, *BATF*, *IFIT3*, and *CD40*, which were consistent with the changes in macrophages with siRNA-mediated knockdown of p21 (Fig. 5 E and Fig. 4 H). Consistent with upregulation of NF-κB–related genes, BMDMs from p21$^{CE}$ showed elevated levels of total and phosphorylated p65 after

withdrawing CSF1 overnight, suggesting enhanced NF-κB activation (Fig. 5 F). Taken together, these data suggest that constitutive p21 expression regulates inflammatory phenotype in macrophage and might repress the potency of tumor immunity.

Next, we examined the impact of constitutive p21 expression in myeloid cells on PDAC progression. We orthotopically implanted KP-2 cells into p21$^{CE}$ and p21$^{WT}$ mice and analyzed tumors at the end point by flow cytometry. Similar to YFP expression patterns in non-tumor-bearing mice, we found in PDAC tissues that the majority of TAMs, monocytes, and neutrophils were YFP⁺, but the vast majority of tumor-infiltrating conventional DCs (cDCs), lymphocytes, and bone marrow progenitors were YFP⁻ (Fig. 5 G). Corresponding to lack of expression in these cells, we found neither significant changes in bone marrow and blood composition, nor in the numbers of cDC1s, cDC2s, natural killer (NK) cells, NK T (NKT) cells, and γδT cells in pancreatic tissues from p21$^{CE}$ tumor-bearing mice (Fig. S3, D–F). Additionally, the number of other myeloid cells that were not largely dependent on proliferation was also not changed in p21$^{CE}$ when compared to p21$^{WT}$ (Fig. S3 F). With constitutive expression of p21, we found a reduction in TAM proliferation, as measured by BrdU, as well as a decrease in total TAM numbers (Fig. 5, H and I). These data suggest that local proliferation of TAMs is necessary to sustain a local TAM pool. Interestingly, while TAM depletion in other studies typically slowed tumor growth (Zhu et al., 2014; Borgoni et al., 2017; Candido et al., 2018), we saw a significant increase in tumor burden in p21$^{CE}$ mice (Fig. 5 J). These data suggest that changes in myeloid phenotype mediated by p21 drive tumor progression. Before evaluating the phenotypic changes of TAMs in p21$^{CE}$ mice, we examined the tumor-promoting effects on other tumor models. Similar to orthotopic KP-2, the PDA.69 PDAC model (Lee et al., 2016) and PyMT mammary tumor model showed decreased TAM proliferations and numbers, but accelerated tumor progression (Fig. 5, K and L). Together, these data suggest that constitutive expression of p21 in myeloid cells reduces TAM proliferations and numbers, but also alters TAM phenotype to drive tumor progression.

### p21 expression in macrophages led to an inflammatory but immunosuppressive phenotype

We next sought to explore how high p21 expression in myeloid cells affected their phenotype in vivo. We conducted scRNAseq analyses on sorted CD45⁺ cells from PDAC tissues in p21$^{WT}$ and p21$^{CE}$ mice. An unsupervised clustering algorithm identified 19 clusters (Fig. S4 A), which mainly included C1qa-expressing macrophages, Ly6C2-expressing monocytes, S100a8-expressing

granulocytes, Cd3d-expressing T cells, and Ms4a1-expressing B cells (Fig. 6 A and Fig. S4 B). To assess transgene expression, we analyzed the expression of YFP sequences. Consistent with flow cytometry data, myeloid compartments, including macrophages, monocytes, neutrophils, and eosinophils, had high YFP expressions, while dendritic cells (DCs) had minimal and non-myeloid cells had no expression (Fig. 6 B).

To more accurately define myeloid subpopulations identified by scRNAseq and evaluate the phenotypic changes in each, starting from TAMs, we computationally separated macrophage/monocyte clusters and reanalyzed these at a higher resolution. This approach generated 17 clusters, which were grouped into four major populations, including macrophages with high MHCII expression (MHCII$^{hi}$ Macs), low MHCII expression (MHCII$^{low}$ Macs), monocytes (Mono, Mono2), and proliferating macrophages (ProMacs; Fig. 6 C). After identifying major macrophage subsets, we first performed cell cycle analysis on all macrophages and confirmed that their proliferations were reduced (Fig. 6 D). Second, we observed that a higher percentage of TAMs in p21$^{CE}$ was in the MHCII$^{low}$ cluster and that this change was also observed at the protein level by flow cytometry (Fig. 6, E and F), indicating that TAMs in p21$^{CE}$ potentially had impaired cross-presentation. In addition, we saw TAMs from p21$^{CE}$ tumor expressed higher level of MHCI, CD40, CD11b, and CD206 by flow cytometry (Fig. S3 G). Third, we performed GSEA between p21$^{CE}$ TAMs and p21$^{WT}$ TAMs and found that consistent with in vitro experiments, TAMs in p21$^{CE}$ were enriched in TNF-α signaling, as well as pathways associated with hypoxia and inflammatory responses (Fig. 6 H and Fig. S5 A). Notably, we also observed downregulation of genes associated with antigen processing and presentation of H2-Aa, H2-Ab1, H2-Eb1, and Cd74, and with the complement components of C1qa, C1qb, and Lyz, whereas tissue-remodeling markers of Arg1, Mmp19, Vegfa, and Mmp9 were upregulated in TAMs from p21$^{CE}$ tumor-bearing mice (>1.5-fold, adjusted P < 0.05; Fig. 6 I). Further, we examined YFP expression, indicating p21-YFP construct expression, and NF-κB signaling across TAM subsets identified in scRNAseq. We observed that expression levels of the p21-YFP construct and enhancement of NF-κB signaling were near ubiquitous across TAMs subsets (Fig S5, C–E). Taken together, these data suggest that TAMs in p21$^{CE}$ are more inflammatory, characterized by high NF-κB signaling, and are more immunosuppressive, characterized by both impaired anti-tumor functions and expressions of M2-like gene signatures. In addition, we found an increase of eosinophils within the TME of PDAC from p21$^{CE}$ tumor-bearing mice (Fig. S4 C), which further illustrated that the TME was more inflammatory.

To confirm that the p21$^{CE}$ model recapitulated the characteristics of p21$^{High}$ TAMs identified in mouse PDAC tissues in Fig. 4 L, we examined the expression levels of p21$^{High}$ gene signature defined in Fig. 4 M in TAMs from p21$^{CE}$ and p21$^{WT}$ tumor-bearing mice. We found that TAMs in p21$^{CE}$ expressed significantly higher levels of the p21$^{High}$ gene signature (Fig. S4 D). In addition, a gene encoded for the common γ chain of the FC receptor (Fcer1g) was significantly reduced in p21$^{High}$ TAMs across three mouse scRNAseq datasets in Fig. 4 M. Cross-linking of FcγRs and the common γ chain is required for IgG-

mediated response and phagocytosis (Castro-Dopico and Clatworthy, 2019). Therefore, we evaluated whether p21$^{CE}$ macrophages had impaired FcγR-mediated phagocytosis. We cultured BMDMs differentiated in medium containing CSF1 from p21$^{CE}$ or p21$^{WT}$ non-tumor-bearing mice with IgG-coated beads and found significantly less phagocytosis in p21$^{CE}$ BMDMs (Fig. 6 G). These data suggest TAMs with high p21 expression have impaired effector functions which could contribute to tumor progression. Finally, we analyzed a gene expression signature derived from TAMs in p21$^{CE}$ mice in human PDAC expression datasets. Our analysis found that the p21$^{CE}$ signature was also associated with "immune escape" signatures (Lin et al., 2007) and poor progression-free survival (Fig. 6, J and K).

To understand the changes in other myeloid cells from p21$^{CE}$ mice, we compared the numbers of significantly changed genes in each myeloid population between the two genotypes. We found that TAMs showed the largest number of DEGs (80 genes), followed by monocytes (34 genes), and only a few genes in neutrophils and granulocytes (Fig. S4 G). These data suggest that macrophages are likely the predominant driver of tumor burden differences. To confirm macrophages contribution to the tumor acceleration in p21$^{CE}$ mice, we administered αCSF1 IgG and clodronate-containing liposomes to p21$^{CE}$ and p21$^{WT}$ tumor-bearing mice throughout tumor development. We found that the number of TAMs was significantly reduced, while the number of monocytes did not after the treatment (Fig. S4, J and K). Only in the setting of macrophage depletion were the tumor promoting effects observed in p21$^{CE}$ mice abolished (Fig. S4 I). Therefore, these data suggest that macrophages are the main driver for tumor acceleration in p21$^{CE}$ mice.

Although YFP was not significantly expressed by DCs, DCs play a critical role in antigen processing and presentation as well as CD8$^+$ T cell activity and could potentially affect tumor progression (Gardner and Ruffell, 2016). To evaluate the changes in DCs in p21$^{CE}$ tumors, we reclustered DC populations from scRNAseq data at a higher resolution and identified seven major subsets: cDC1, cDC2a, cDC2b, migratory DC, plasmacytoid DC (pDC), and proliferating cDC1 and cDC2 (Fig. S4 E). The cDC1 expressed classical DC1 markers of Xcr1, Clec9a, and also Baft3 and Irf8, while the cDC2 subsets expressed Cd11b, Irf4, and Sirpa, and were further separated into cDC2a and cDC2b based on Epcam expression (Merad et al., 2013; Kaplan, 2017). We did not observe significant changes in the percentages of cDC1s, cDC2s, migratory DCs, and proliferating DCs as the total number of DCs between two genotypes, nor did we observe a change in genes associated with cross-presentation. We saw a decrease in pDCs and an increase of cDC2bs as the percentage of total DCs (Fig. S4 F). Because pDCs are one of the major producers of type I IFN (Koucký et al., 2019) and could potentially drive anti-tumor immunity, this reduction could also contribute to tumor immune suppression.

## p21 expression in macrophages impaired effector T cells
To determine whether impaired antigen processing and presentation in macrophages directly affected T cell numbers and functions, we reanalyzed T cell clusters from the scRNAseq experiment at a higher resolution. Unsupervised clustering generated 12 clusters
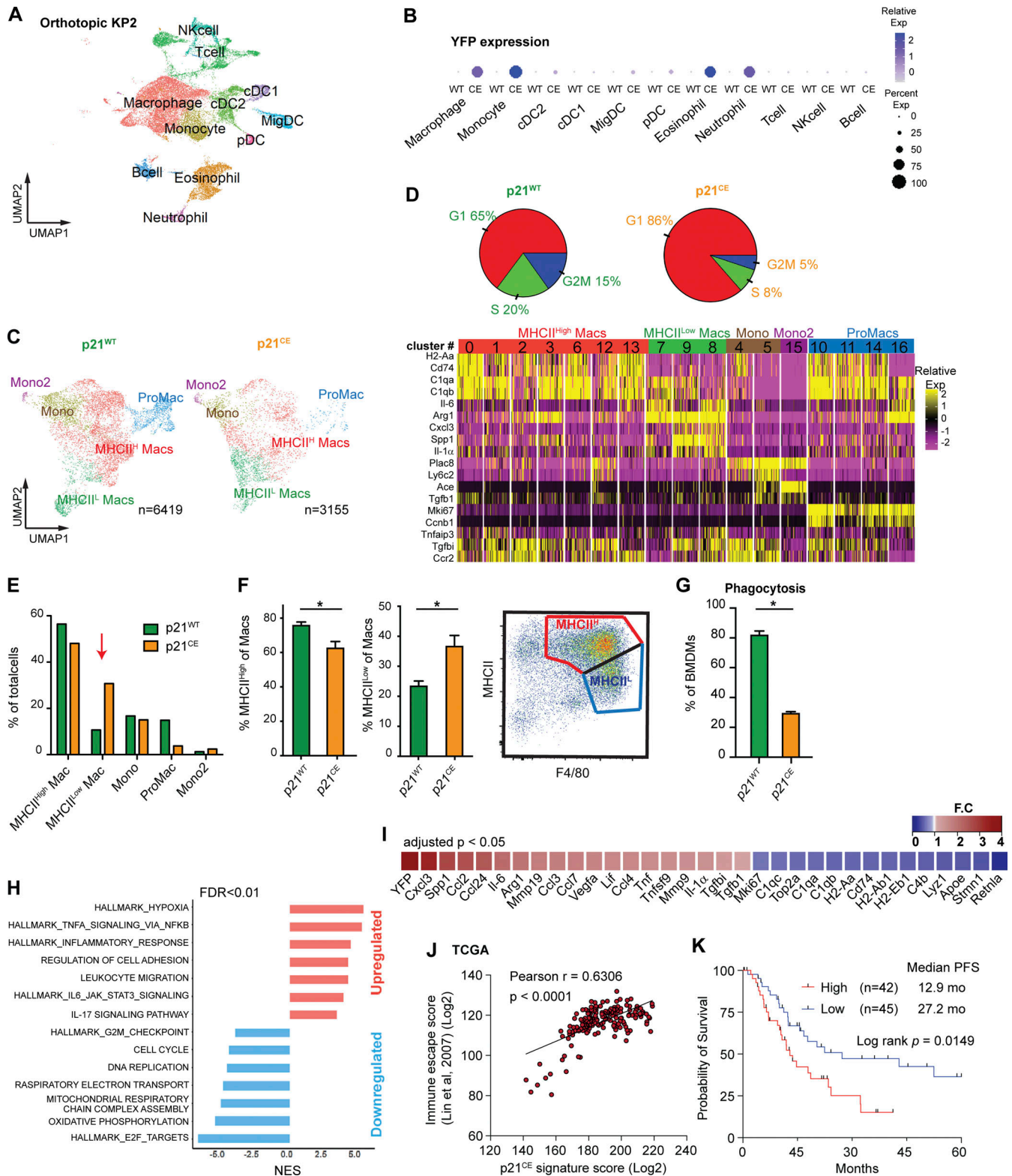
Zuo et al.
Macrophage proliferation and immune suppression

Journal of Experimental Medicine
https://doi.org/10.1084/jem.20212062

11 of 23

Figure 6. **p21 expression in macrophages led to an inflammatory but immunosuppressive phenotype. (A)** UMAP dimensionality reduction plot of total CD45^{+} cells from p21[WT] and p21[CE] mice bearing orthotopic KP-2 tumors. Cells in each genotype were pooled from three mice and created as two libraries. Clusters were annotated with corresponding cell types. **(B)** Dot plot displaying YFP expression in each cell type between the two groups. The legend shows the dot size and corresponding percentage that are expressed as a color gradient of normalized expressions. **(C)** Reclustered UMAP plot of macrophage and monocyte clusters in A without cell cycle regression and split into p21[WT] and p21[CE] and annotated with major subpopulations. On the right, heat map showing key gene expressions in each subpopulation in C. **(D)** Pie chart showing cell cycle analysis of macrophages (MHCII[hi], MHCII[low], and ProMac) in tumors from p21[WT] and p21[CE] mice. **(E)** Bar plot showing quantification of each population between p21[WT] and p21[CE] mice identified in C. **(F)** Quantification of flow

cytometry analysis of the percentages of MHCII$^{hi}$ and MHCII$^{low}$ macrophages from p21$^{CE}$ and p21$^{WT}$ mice bearing orthotopic KP-2 tumors with the representative gating strategy; $n$ = 6–10 mice/group. Data were consistent in four independent repeats. **(G)** Bar plot displaying quantification of fluorescent-bead$^{+}$ BMDMs from p21$^{WT}$ and p21$^{CE}$ mice. Data were consistent in three independent repeats. **(H)** Bar plot displaying GSEA results of comparing TAMs from p21$^{CE}$ to p21$^{WT}$ mice. The key upregulated and downregulated pathways are shown with FDR <0.01. **(I)** Heat map showing the key DEGs comparing TAMs from p21$^{CE}$ and p21$^{WT}$ mice. DEGs were filtered with an adjusted P < 0.05 and fold-change >1.3 or <0.75. All gene expressions were normalized by SCTransform. **(J)** Correlation plots with Pearson coefficients (r) of p21$^{CE}$ signature score (included genes with logFC > 0.75) vs. immune escape score from TCGA PDAC PanCancer Atlas study ($n$ = 180). **(K)** Kaplan–Meier survival analysis of PDA patients from TCGA whose samples were stratified by expression of the p21$^{CE}$ signature (logFC > 0.75) by quartiles. All graphs are expressed as the mean ± SEM. *, P < 0.05 using the $t$ test, except for I where the Bonferroni-corrected adjusted P value was used.

and were manually assigned into NK cells, Tregs, two clusters of CD4$^{+}$ (CD4#1 and CD4#2), two clusters of CD8$^{+}$ (CD8#1 and CD8#2), double negative T cells, and a γδ T cell based on known cell type markers (Fig. 7 A). Among CD8$^{+}$ T cells, cluster #2 expressed the higher effector genes, *Gzma*, *Gzmb*, and *Cd74*, and therefore was considered as cytotoxic effectors (Fig. 7 A). We observed that this CD8$^{+}$ effector cluster was reduced as a percentage in p21$^{CE}$ tumor-bearing mice (Fig. 7 B) and the expressions of effector genes, *Gzma*, *Gzmk*, and *Klrg1*, were also significantly lower (Fig. 7 D). In contrast, we saw an increase in the percentage of CD4#2 T cell populations, which are T$_{H}$2 polarized, with high levels of *Gata3*, *IL-4*, and *IL-13* (Fig. 7 A; Zheng and Flavell, 1997). If mapping the upregulated genes in cytotoxic CD8$^{+}$ T cells from p21$^{CE}$ tumors to known signaling pathways, we found enrichment in apoptosis and IL-2-STAT5 signaling, suggesting overexpressed p21 in macrophages may cause more cytotoxic CD8$^{+}$ T cell death (Fig. 7 C). To confirm this, we co-cultured CD3/CD28 bead–activated CD8$^{+}$ T cells with BMDMs generated from p21$^{CE}$ and p21$^{WT}$ mice in vitro and found p21$^{CE}$ BMDMs led to more 7AAD$^{+}$ CD8$^{+}$ T cells (Fig. S4 H).

To corroborate these findings, we used a T cell–focused CyTOF panel. CD45$^{+}$TCRβ$^{+}$CD90$^{+}$NK1.1$^{-}$TCR-γδT$^{-}$ cells were selected for further clustering based on 20 T cell functional markers. This approach generated 18 clusters that could be mainly grouped into three major populations: CD4$^{+}$ T cells, regulatory CD4$^{+}$ T cells (Tregs), and CD8$^{+}$ T cells (Fig. 7, E and F). We next evaluated changes in each subpopulation and found a significant decrease in the numbers of cytotoxic effectors (cluster 4), which expressed high levels of granzyme B and KLRG1, and also an expansion of the CD4$^{+}$ Treg (cluster 5) that expressed high levels of PD1 (Fig. 7 G). In addition, we found that CD8$^{+}$ T cells as a whole in p21$^{CE}$ tumors expressed lower levels of KLRG1 and CD90, but higher levels of CD44, Tim3, and PD1, indicating a more exhausted and less functional phenotype (Fig. 7 H). Consistent with impaired effector functions, we observed a significant decrease in the percentage of CD8$^{+}$ T cells that express IFNγ and TNF-α from p21$^{CE}$ orthotopic tumors when compared to from p21$^{WT}$. We also observed a similar reduction in IFNγ$^{+}$ T cells when co-cultured with BMDMs from p21$^{CE}$ mice in comparison with p21$^{WT}$ (Fig. 7, J and K). Inhibition of NF-κB impaired p21$^{CE}$ BMDMs ability to repress T cell effector functions (Fig. S4 L). These data suggest that chronic activation of NF-κB in p21$^{CE}$ macrophages can drive their T cell suppressive phenotype. To extend the findings to human PDAC patients, we analyzed the correlations between the p21$^{CE}$ signature in TAMs with T cell exhaustion (Tirosh et al., 2016) and found strong positive correlations (Fig. 7 I).

Taken together, these data suggest high p21 expression in TAMs drives chronic activation of NF-κB and T cell dysfunction. Finally, to determine whether accelerated tumor progression in p21$^{CE}$ mice was driven by T cells, we depleted CD8$^{+}$ T cells in both p21$^{CE}$ and p21$^{WT}$ mice through injection of αCD8 IgG. We no longer observed difference in tumor burdens between the two groups (Fig. 7 L). These data suggest that p21-driven TAM immunosuppressive phenotype not only reduces the number of anti-tumor T cells but also impairs the functions of remaining T cells.

As we saw increased expression of CD40 in TAMs from both GEMM KPC and orthotopic models (Fig. 8, A and C), we next asked whether innate immune agonist therapy, CD40 agonist, could re-educate TAMs and restore their effector functions (Coveler et al., 2020). To test this, we treated p21$^{CE}$ and p21$^{WT}$ mice bearing orthotopic KP-2 tumors with CD40 agonist plus gemcitabine and found that while the dual treatment had limited effect on p21$^{WT}$ mice, it dramatically reduced the tumor burden in p21$^{CE}$ mice and increased CD8$^{+}$ T cell infiltration (Fig. 8, B and D). These data suggest, although stromal or chemo-induced p21 expression drives an inflammatory and immunosuppressive phenotype in TAMs, these same pathways may make tumor uniquely susceptible to CD40 agonist therapy.

## Discussion

Macrophage proliferation has been observed in several non-cancer pathological conditions, including helminth infections (Jenkins et al., 2011), atherosclerosis (Tang et al., 2015), and obesity-associated adipose tissues (Amano et al., 2014). In these conditions, proliferation of macrophages, albeit under the control of different factors, is necessary to sustain total macrophage numbers at each tissue site. In our studies, we found in pancreatic tumors that macrophage proliferation was mainly driven by CAF-derived CSF1. These data implied that although the general need for macrophage expansion was common, the activated signaling pathways and resulting macrophage phenotypes were largely tissue- and context-dependent. Stromal-rich tumors may increase TAM numbers more frequently by local proliferation. Interestingly, CSF1 levels were reported to be higher in the blood of patients suffering from melanoma, breast cancer, or pancreatic cancer. In these patients and also in corresponding mouse models, macrophages were found to be proliferative (Bottazzi et al., 1990; Franklin et al., 2014; Tymoszuk et al., 2014). These data suggested that CSF1-driven macrophage proliferation was common in multiple cancer types.

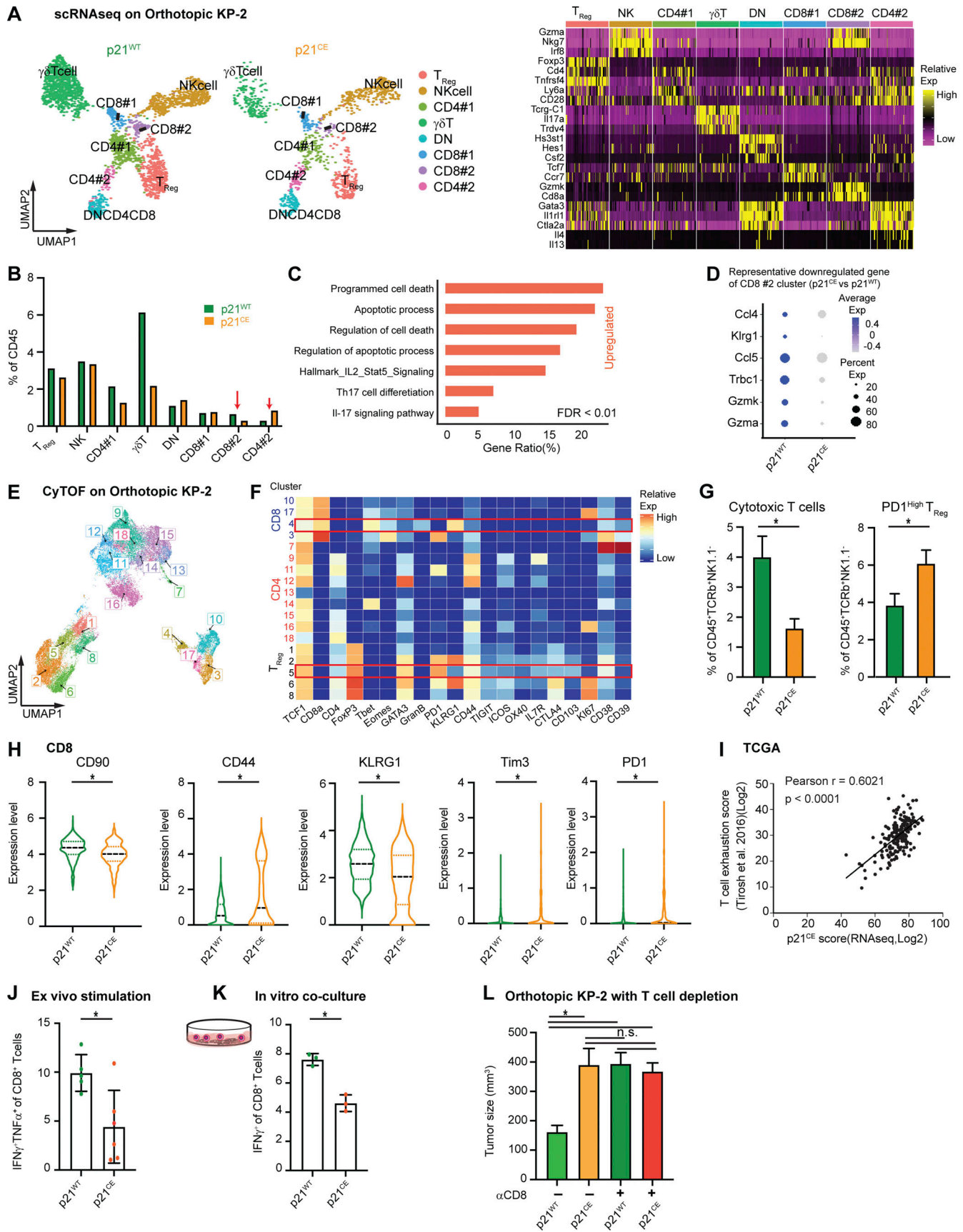An earlier study examined the CSF1 effects on CSF1R-expressing human breast cancer cell lines and found that CSF1

Figure 7. **p21 expression in macrophages impaired effector T cells. (A)** UMAP dimensionality reduction plot of selected lymphocytes (clusters 6, 7, 8, 13, and 17 in Fig. S4, A and B) from p21[WT] and p21[CE] orthotopic KP-2 tumors. Clusters were annotated with corresponding cell types and heat maps displaying

selected gene expressions in each cell type. **(B)** Bar graph displaying the composition of each cell type as the percentage of total CD45$^+$ cells in p21$^{WT}$ and p21$^{CE}$ tumor-bearing mice. CD8#2 and CD4#2 are highlighted with red arrows. **(C)** Bar graph displaying the upregulated pathways in the CD8#2 cluster from p21$^{CE}$ using overrepresentation analysis of DEGs to known biological functions (GO, KEGG, Reactome, and the MSigDB). DEGs were filtered with a value of $P < 0.05$, fold-change >1.2, and past MAST test. **(D)** Table showing the DEGs comparing CD8#2 cluster from p21$^{CE}$ to p21$^{WT}$ with $P$ value <0.05. **(E)** UMAP plot of selected CD45$^+$TCRβ$^+$CD90$^+$NK1.1$^-$TCR$^-$γδT$^-$ cells from p21$^{CE}$ and p21$^{WT}$ orthotopic KP-2 tumors with clusters annotated; $n = 7$ mice/group. **(F)** Heat map displaying the feature expressions in each cluster. Cytotoxic T cells (cluster 4) and PD1$^{High}$ Treg (cluster 5) were highlighted. **(G)** Bar plot showing the percentages of cytotoxic T cells and PD1$^{High}$ Treg in p21$^{WT}$ and p21$^{CE}$ tumors. **(H)** Violin plot visualizing the expression levels of CD90, CD44, KLRG1, TIM3, and PD1 in the CD8 cluster between tumors from two genotypes. **(I)** Correlation plots with Pearson coefficients ($r$) of p21$^{CE}$ score vs. T cell exhaustion score from TCGA PDAC PanCancer Atlas study ($n = 180$). **(J)** Bar graph displaying the percentage of IFNγTNFα$^+$ effector CD8 T cells as total CD8 in p21$^{WT}$ and p21$^{CE}$ tumors; $n = 5$–6 mice/group, two independent experiments. **(K)** Bar graph displaying the percentage of IFNγ$^+$ activated CD8 T cells when co-cultured with BMDMs from p21$^{WT}$ and p21$^{CE}$ mice; $n = 3$, three independent experiments. **(L)** Bar graphs showing the tumor burden between p21$^{WT}$ and p21$^{CE}$ orthotopic KP-2 tumors after αCD8 treatment; $n = 6$–8 mice/group, two agreeing independent experiments. All graphs are expressed as the mean ± SEM. *, $P < 0.05$; for comparisons between two groups (G and I–L), Student's two-tailed $t$ test was used. For comparisons in H, the Bonferroni-corrected $P$ value was used.

inhibited cell proliferation through inducing p53-independent, but MAPK-dependent, p21 expression (Lee et al., 1999). This result may seem contradictory to ours as we showed CSF1-induced BMDM proliferation. However, we also showed that knocking down p21 expression or constitutively expressing it promoted or inhibited macrophage proliferation. These data suggested that CSF1 induction of p21 in macrophages acted as a checkpoint for S phase entry. The ultimate cell cycle transit required additional signaling, and the signals could be synthesized according to the expression level of p21. One group reported that Raf signal intensity determined either induction of DNA synthesis or inhibition of proliferation in fibroblasts by p21$^{Cip1}$ expression levels (Sewing et al., 1997). A recent study further showed that p21 not only determined the cell cycle fate of mother cells but could also be carried into daughter cells and regulated the proliferation after mitosis (Yang et al., 2017). Therefore, it is not surprising that the p21 expression level is known to protect cells from chemotherapy-induced apoptosis (Hsu et al., 2019). Notably, prolonged CSF1/CSF1R blockade

resulted in rebound myelopoiesis (Kumar et al., 2017; Karmaus et al., 2017), which might complicate the therapeutic impact of this approach to overcome immune suppression.

Aside from p21's canonical role as a cell cycle checkpoint, several groups reported its role in regulating inflammation, with some contradictory results. One group demonstrated that p21$^{-/-}$ mice were more sensitive to LPS-induced septic shock due to inflammation (Trakala et al., 2009). Likewise, p21$^{-/-}$ mice showed enhanced experimental inflammatory arthritis and severe articular destruction (Mavers et al., 2012). Contrastingly, in a serum transfer model of arthritis, p21$^{-/-}$ mice were more resistant (Scatizzi et al., 2006). Furthermore, disruption of p21 attenuated lung inflammation in mice (Yao et al., 2008). These data suggested that regardless of whether p21 promoted or inhibited inflammation, it was established that p21 regulated inflammation. In a chronic pancreatitis model, one study found that p21 expression was significantly increased overall, while knocking down its expression resolved inflammation and prevented pancreatic injury through reducing the release
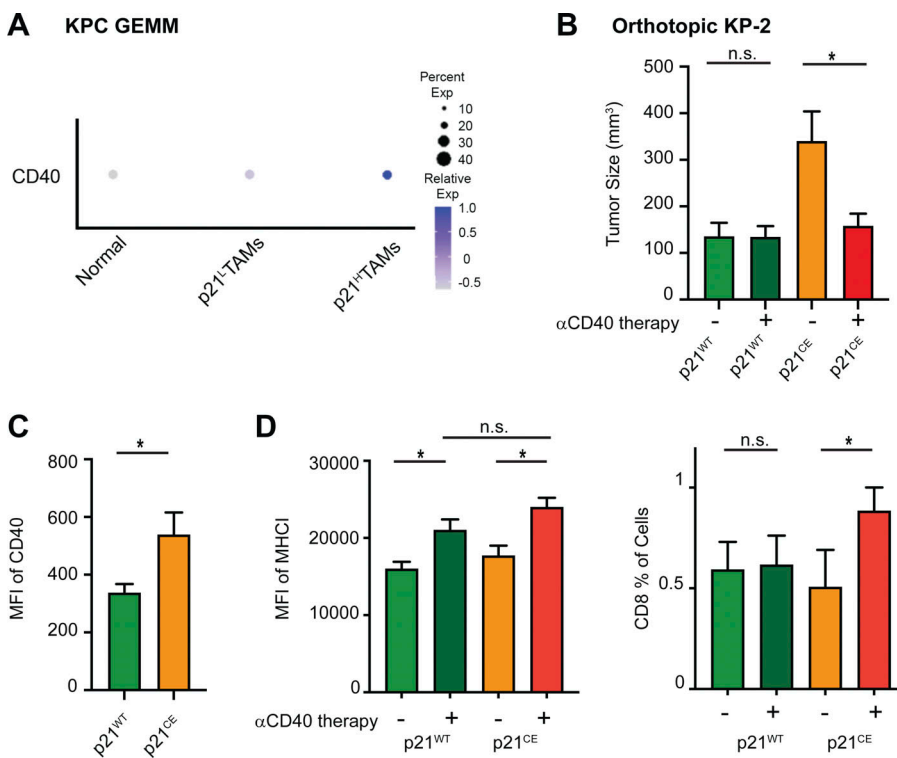


**Figure 8. p21 expression in macrophages sensitizes tumors for innate immunotherapy. (A)** Dot plot showing average expression of CD40 in macrophages from normal pancreas and in TAMs from KPC tumors. Dot size representing the percent of cells expressing CD40. **(B)** Bar graph showing the tumor burdens of p21$^{WT}$ and p21$^{CE}$ mice bearing orthotopic KP-2 tumors with or without CD40 agonist (100 µg) and gemcitabine (75 mg/kg) treatment. $n = 6$–8 mice/group. Data were consistent in two independent repeats. **(C)** Bar graph showing the mean fluorescent intensity (MFI) of CD40 in TAMs from p21$^{WT}$ and p21$^{CE}$ mice bearing orthotopic KP-2 tumors. **(D)** Bar graphs showing the MFI of MHCI in TAMs and the percentage of CD8 as of total cells from p21$^{WT}$ and p21$^{CE}$ mice bearing orthotopic KP-2 tumors. All graphs are expressed as the mean ± SEM. *, $P < 0.05$ for comparisons between two groups; Student's two-tailed $t$ test was used.

Zuo et al.
Macrophage proliferation and immune suppression

Journal of Experimental Medicine    15 of 23
https://doi.org/10.1084/jem.20212062

of NF-κB–mediated proinflammatory cytokines, such as TNF-α, IL-6, and CXCL1 (Seleznik et al., 2018). These data suggested that at least in the pancreas, p21 played a role in promoting inflammation, independent of KRAS mutations that are commonly observed in PDAC and are known to drive inflammation (Kitajima et al., 2016). However, this study did not identify the main drivers for p21-mediated inflammation.

Macrophages are known to exhibit plasticity, which gives them the capability to quickly respond to environmental challenges. The expression levels of p21 could be an important regulator in macrophage plasticity. Expression of p21 inhibited macrophage activation during LPS-induced septic shock, as p21$^{-/-}$ macrophage expressed higher levels of CD40 and enhanced activation of NF-κB (Trakala et al., 2009). One study further demonstrated that the expression of p21 acted more like a buffer system for inflammation as it could adjust the equilibrium between p65-p50 and p50-p50 NF-κB pathways to mediate macrophage plasticity in LPS treatment (Rackov et al., 2016). However, none of these studies investigated p21 effects on macrophage polarization in tumor settings. From scRNAseq data, we showed that stratifying macrophages based on p21 expressions into p21$^{Hi}$ and p21$^{Low}$ resulted in two phenotypically distinct macrophages independent of the cell cycle, with the first being more inflammatory. TNF-α and NF-κB were upregulated when p21 expression was high, which is consistent with previous findings. We further illustrated that constitutive expression of p21 in macrophages impaired their phagocytosis capabilities in vitro, lowered expression of genes associated with antigen cross-presentation in orthotopic PDAC tumors, and hindered cytotoxic T cell functions, which eventually led to faster tumor progression. These observations are important because as we showed both stromal interaction and therapeutic interventions targeting cell cycle could induce p21 expression in TAMs and lead to an inflammatory yet immunosuppressive phenotype. Given that TAMs are usually abundant in TME, these p21-driven phenotypic changes could eventually lead to resistance for treatments.

We also found that in human and mouse PDACs, although p21 expression was highest in macrophages, it was expressed by other myeloid populations. If p21 regulates inflammatory responses through NF-κB in macrophages, it is possible that other immune cells mediate inflammation, like granulocytes and neutrophils, which could also be polarized by p21 in a similar way. One group observed that p21 expression in neutrophils regulated inflammation in infections (Martin et al., 2016). In addition, we observed that p21 expression was induced by chemotherapy not only in macrophages but also in other myeloid cells, which suggested that inflammatory but immunosuppressive phenotypes could be further strengthened by myeloid cells, in addition to macrophages.

Understanding how the TME and cancer cell–intrinsic factors regulate macrophage tumor–supportive vs. tumor–suppressive functions is critical to therapeutically targeting TAMs in cancer patients. In total, our data suggested that CAF-induced macrophage proliferation was important for sustaining TAM number and induction of p21, which also resulted in immunosuppression and tumor progression. Lastly, expression of p21 in TAMs might sensitize tumors to CD40 agonist treatment.

# Materials and methods
## Contact for reagent and resource sharing
Further information and requests for resources and reagents should be directed to and will be fulfilled by the lead contact, David G. DeNardo (ddenardo@wustl.edu).

## Murine PDAC models
Mice were maintained in the Laboratory for Animal Care barrier facility at the Washington University School of Medicine. All studies were approved by the Washington University School of Medicine Institutional Animal Studies Committee.

KPC mice used in these studies have been rapidly bred to the C57Bl/6J background in our laboratory using speed congenics and further backcrossed more than five times. All mice were housed, bred, and maintained under specific pathogen–free conditions in accordance with the National Institutes of Health American Association for Laboratory Animal Care standards and were consistent with the Washington University School of Medicine institutional animal care and use committee regulations (protocols #20160265 and #19-0856).

The KP-1 cell line was derived from PDAC tissues of the 2.2-mo-old (KPC); the KP-2 cell line was derived from the 6-mo-old p48-CRE$^+$/LSL-Kras$^{G12D}$/p53$^{flox/+}$ mice (KP$^{fl/+}$C; Jiang et al., 2016). The KI cell line was derived from the Pdx1-Cre;LSL-Kras$^{G12D}$;Ink/Arf$^{fl/fl}$ as previously described (Mitchem et al., 2013). Cells were grown on collagen-coated tissue culture flasks for <12 passages and were tested for cytokeratin-19, smooth muscle actin, vimentin, and CD45 to verify their carcinoma identity and purity. The PDA.69 cell line was a kind gift from Dr. Gregory L. Beatty (University of Pennsylvania, Philadelphia, PA, USA) and was maintained in tissue culture flasks with DMEM supplemented with 1% glutamax and 0.167% gentamycin for <13 passages. To establish orthotopic PDAC models, either 50,000 or 200,000 KP-2 cells, and 10,000 or 50,000 PDA.69 cells in 50 μl of Cultrex (Trevigen) were injected into the pancreas of 8–12-wk-old C57BL/6 mice or transgenic mice according to published protocols (Kim et al., 2009). Tumor-bearing mice were sacrificed when the palpable tumor size was >1 cm (21–27 d).

## Other mouse models
The p21$^{CE}$ mouse was developed at the Washington University Mouse Embryonic Stem Cell Core using the construct of Cdkn1a (p21, accession no. NM_007669). Briefly, the construct contained the p21 gene under the control of a CAG promoter and a lox-stop-lox case. Downstream of the p21 gene, the construct also contained an IRES and YFP gene for visualization. The construct was then integrated into the ROSA locus of pure C57/B6 mice (ROSA-CAG-LSL-p21-IRES-YFP) and injected into C57 blastocyst (p21$^{+/wt}$). Successful chimeras were selected and verified by DNA sequencing across ROSA junctions (primers are listed in Table S2), and subsequent founder mice were identified through genomic PCR (primers are listed in Table S2). Then, p21$^{+/wt}$ mice were crossed with LysMCre mice to specifically induce p21 expression in macrophages. The resulting LysM$^{+/+}$/p21$^{+/wt}$ mice are termed "p21 constitutive expression" (p21$^{CE}$) mice.

## Tissue harvest

Mice were euthanized by intracardiac perfusion with 15 ml of PBS-heparin under isoflurane anesthesia. Blood was obtained by cardiac puncture and deposited in heparin-PBS (Alfa Aesar Lonza) solution. Blood was then incubated in red blood cell lysis buffer (BioLegend) for 10 min on ice and quenched with 1% FBS (Atlanta Biologicals) containing PBS. Normal and tumor tissues were manually minced and digested in 20 ml of Hank's balanced salt solution (Thermo Fisher Scientific) supplemented with 2 mg/ml of collagenase A (Roche) and 1× DNase I (Sigma-Aldrich) for 30 min (20 min for normal tissue) at 37°C with agitation. After digestion, the cell suspensions were quenched with 5 ml of PBS and filtered through 40-µm nylon mesh. The filtered suspensions were then pelleted by centrifugation (1,800 rpm for 4 min at 4°C) and resuspended in flow cytometry buffer PBS containing 1% BSA and 5 mM EDTA as a single-cell suspension.

## Flow cytometry

Following tissue digestion, single-cell suspensions were blocked with rat anti-mouse CD16/CD32 antibodies (eBioscience) for 10 min on ice and pelleted by centrifugation. The cells were subsequently labeled with 100 µl of fluorophore-conjugated anti-mouse extracellular antibodies at recommended dilutions for 30 min on ice in flow cytometry buffer. Intracellular staining was conducted using eBioscience Transcription Factor Staining Buffer using the manufacturer's recommended procedures. All antibodies are listed in Table S2. For live analysis of YFP, fluorophore-labeled cells were analyzed immediately without fixation on X-20 cytometers. For proliferation assays, mice were injected with BrdU, 1 mg i.p. at 3 h prior to sacrifice. A BD Biosciences Cytofix/Cytoperm kit (BD Biosciences) was used following extracellular staining to stain for BrdU.

To measure T cell cytokine productions in vitro, primary cell suspension containing 100,000 naive CD8 T cells were incubated in 96-well with 1 µM brefeldin A (BioLegend) and 2 µM Monensin solution (BioLegend) and 1× stimulation cocktail (eBioscience) and 400,000 BMDMs from p21$^{CE}$ and p21$^{WT}$ mice for 4 h at 37°C and 5% $CO_2$. For addition of NF-$\kappa$B inhibitor, BMDMs from p21$^{CE}$ and p21$^{WT}$ mice were cultured overnight with or without BAY11-7082 (10 µM) prior to co-culture with CD8$^+$ T cells. For experiments that measured T cell cytokines involving ex vivo stimulation, following tissue digestion, 1 million cells were stimulated as described above for 4 h. After incubation, cells were resuspended in Fc block buffer and then labeled with fluorophore-conjugated anti-mouse antibodies as above.

## Human samples

Human PDAC samples were obtained from consenting patients diagnosed at Washington University and the Siteman Cancer Center. Patients underwent pancreaticoduodenectomy. The Washington University Ethics committee approved the study under Institutional Review Board protocol #201704078.

## Mass cytometry

Human tumor samples were collected on different days right after surgery and digested in Hank's balanced salt solution supplemented with 2 mg/ml collagenase A (Roche), 2.5 U/ml hyaluronidase (Sigma-Aldrich), and DNase I at 37°C for 30 min with agitation to generate single-cell suspensions. Cell suspensions were counted and stained in 5 µM cisplatin per million cells for exactly 3 min on ice and washed with Cy-FACS buffer (PBS, 0.1% BSA, 0.02% NaN$_3$, and 2 mM EDTA) twice. The cells were then incubated with FcR blocking reagent plus surface-antibody cocktail for 40 min on ice. After incubation, surface marker–stained cells were washed twice with Cy-FACS buffer. Cells were then fixed with 4% paraformaldehyde (PFA) for 10 min on ice and permeabilized with permeabilization buffer containing the intracellular stain cocktail (Invitrogen) for 40 min. All antibodies are listed in Table S2. The cells were then washed and fixed a second time in 4% PFA in PBS at 4°C at least overnight. 1 d prior to acquisition, the cells were washed twice and stained with 200 µl of DNA intercalator per million cells. Cells were acquired on a CyTOF2 mass cytometer and were normalized with the MATLAB normalizer (v.7.14.0.739 run in MATLAB R2012a; Finck et al., 2013). The normalized data were uploaded into Cytobank and manually gated to exclude normalization beads, cell debris, dead cells, doublets, and CD45$^-$ cells. The filtered sample from each individual specimen was then exported and batch normalized by the date of acquisition using the R Cydar package NormalizeBatch function (mode = "range") to compute a quantile function from the pooled distribution of the input expression data (Lun et al., 2017). In brief, batch expression was scaled between the upper and lower bounds of the pooled reference distribution, with zero values fixed at zero. A total of 10,245 events per batch of corrected sample were then visualized using the standard t-distributed stochastic neighbor embedding (t-SNE) algorithm in Cytobank. Populations of interest were manually gated and verified based on lineage marker expressions.

For mouse samples in Fig. 7, F–I, seven mice per group were individually stained for surface and intracellular stains (the antibodies are listed in Table S2) and fixed overnight as described above. Each sample was then barcoded with a unique combination of palladium metal barcodes using the manufacturer's instructions (Fluidigm). Following bar coding, the cells were pooled together and incubated overnight in 2% PFA containing 40 nM iridium nucleic acid intercalator (Fluidigm). On the day of acquisition, the barcoded samples were washed and suspended in water containing 10% EQ Calibration Beads (Fluidigm) before acquisition on a CyTOF2 mass cytometer (Fluidigm). Sample barcodes were interpreted using a single-cell debarcoder tool (Zunder et al., 2015). FCS files were then uploaded to Cytobank and manually gated to exclude normalization beads, cell debris, dead cells, and doublets. Classical T cells were classified as CD45$^+$, Cisplatin$^-$, Thy1.2$^+$, NK1.1$^-$, TCR$\gamma\delta^-$, and TCR$\beta^+$. All T cells were exported as new FCS files and analyzed using the R CATALYST package (Nowicka et al., 2017) in R, v.3.8.2 (The R Project for Statistical Computing). In brief, FCS files were downsampled to equivalent cell counts, before clustering with the R implementation of the Phenograph algorithm (Levine et al., 2015). All markers were used for clustering analysis except markers used for T cell gating (see above). Dimensional reduction and visualization were performed using

the UMAP algorithm (McInnes et al., 2020). Finally, differential cluster abundance testing was performed with the R diffcyt package, utilizing a generalized linear mixed model (Weber et al., 2019).

### Macrophage and T cell depletion
In Fig. 3 E, 8–12-wk-old C57BL/6 mice were orthotopically implanted with 200,000 KP-2 cells. When the tumor was palpable, mice were intraperitoneally treated with one dose of 1 mg CSF1-neutralizing antibody (clone 5A1; BioXCell) and sacrificed at 12 and 24 h after treatments.

In Fig. S4, I–K, to deplete tissue-resident macrophages, 8–12-wk-old p21$^{CE}$ and p21$^{WT}$ mice were implanted orthotopically with 50,000 KP-2 cells on day 0, then were treated with three doses of CSF1-neutralizing antibody (1, 0.5, and 0.5 mg on days 3, 10, and 17) and two doses of clodronate-containing liposomes (200 μl each on days 5 and 12). Control mice were treated with the same doses/volumes of IgG (clone HRPN, BioXCell) and PBS liposomes.

In Fig. 7 L, CD8-neutralizing IgG antibodies (anti-mCD8 clone 2.43; BioXCell) were administered intraperitoneally to 8–12-wk-old p21$^{CE}$ and p21$^{WT}$ mice starting 1 d prior to orthotopic implantation with 50,000 KP-2 cells, with the first injection containing 400 μg and subsequent injections (every 4 d) containing 200 μg of each IgG throughout tumor development (i.p.).

### Chemotherapy and innate immunotherapy
In Fig. 4 O, BMDMs from B6 mice were treated with 3 or 30 μM of paclitaxel, 3 or 30 μM of oxaliplatin, 3 μM of Sn38, or 3 μM of 5-FU, respectively, for 24 h. In Fig. 4 P, KPC GEMM were treated with a combination of 50 mg/kg of gemcitabine and 5 mg/kg paclitaxel (i.v.) every 5 d upon on palpation. In Fig. 8 B, p21$^{CE}$ and p21$^{WT}$ mice bearing orthotopic KPC tumor were treated with 75 mg/kg of gemcitabine (i.v.) every 7 d starting on day 7 after implantation and 100 μg of αCD40 (clone FGK4.5, BioXcell) via i.p. injection every 7 d starting on day 9.

### In vitro co-culture and siRNA treatment
All cell lines were maintained in DMEM (Lonza) supplemented with 10% FBS (Atlanta Biological) and penicillin/streptomycin (Gibco). All cell lines tested negative for mycoplasma.

Pancreatic fibroblasts were harvested from the pancreas of healthy 8-wk-old C57BL/6 mice, passaged three times on tissue culture plates, and tested negative for mycoplasma. An immortal pancreatic fibroblast cell line was established by passage more than 18 times. Soluble factors in primary pancreatic fibroblasts and immortal pancreatic fibroblasts medium were measured, compared, and found to be similar. Bone marrow cells were obtained from both femur and tibia of the mouse and differentiated for 5 d in DMEM supplemented with 10 ng of CSF1 (PeproTech) for 5 d to generate BMDMs.

A total of 75,000 fibroblasts or 50,000 KP-2 cells or both cell types were co-cultured with 100,000 BMDMs in 6-well cell culture plates (Costar). BrdU was added 6 h prior to harvest at each time point. For transwell assays, 150,000 fibroblasts were cultured in the transwell assay with 200,000 BMDMs, and BrdU was added 6 h prior to harvest.

siRNAs targeting mouse CSF1 and p21 were purchased from Integrated DNA Technologies. Sequences are listed in Table S2. The siRNA transfections for primary BMDMs and pancreatic fibroblasts were performed using the Mouse Macrophage Nucleofector Kit (Lonza) and Nucleofector 2b Device (Lonza) with prewritten program Y-001 for BMDMs and V-013 for fibroblasts, following the manufacturer's instructions. RNA and protein from transfected primary cells were harvest 24 h after the transfections.

### Microarray and RT-qPCR analysis
Total RNA was isolated from BMDMs derived from p21$^{CE}$, p21$^{WT}$, or p21$^{-/-}$, or from siRNA targeting for p21-treated BMDMs using the E.N.Z.A. Total RNA Kit (Omega Chemicals) according to the manufacturer's instructions. Microarrays were performed on p21 knocked-down BMDMs with the treatment of tumor-conditioned medium for 24 h. A differential gene list was generated with detected fold-changes >1.5, adjusted $P < 0.05$. The filtered differential gene list was loaded into R and a hypergeometric test was used to compare known catalogs of functional annotations (enricher) with a false discovery rate (FDR) of $P < 0.05$. Top differentially regulated genes are listed in Table S1. RNAs from BMDMs of p21$^{CE}$, p21$^{WT}$, and p21$^{-/-}$ were reversed-transcribed to cDNAs by using the qScript cDNA SuperMix (QuantaBio). RT-qPCR Taqman primer probe sets specific for targets listed in Table S2 (Applied Biosystems) were used, and the relative gene expression for each target was determined on a ABI7900HT quantitative PCR machine (Applied Biosystems) using a Taqman Gene Expression Master Mix (Applied Biosystems). The threshold cycle method was used to determine fold-changes of gene expressions normalized to *Gapdh*, *Hprt*, and *Tbp*.

### ELISA and the cytokine array
Conditioned media from fibroblasts and tumor cells were harvested after changing the medium to 0.1% FBS for 24 h with >80% confluency. The cytokine array was conducted using a Proteome Profiler Mouse XL Cytokine Array kit (R&D Systems) following the manufacturer's instructions. The membranes from each conditioned medium were placed in an autoradiography film cassette and exposed to x-ray filming for 5–8 min. Positive signals were quantified by ImageJ software (National Institutes of Health. Conditioned media were concentrated using a Pierce Concentrator (Thermo Fisher Scientific) based on the manufacturer's instructions. CSF1 levels were measured by a Mouse M-CSF Matched Antibody Pair Kit (ab218788) following the manufacturer's instructions.

### scRNAseq
Normal pancreas tissues were taken from three 10-wk-old B6 mice, processed to single-cell suspension as explained in the tissue harvest section, pooled together, and sorted for live macrophages (CD45$^+$CD11b$^+$F4/80$^+$CD3$^-$CD19$^-$Siglecf$^-$Ly6G$^-$Ly6C$^-$7AAD$^-$) using an Aria II cell sorter (BD Biosciences).

Pancreatic tumors were taken from three 1.5-mo-old KPC mice, processed to a single-cell suspension, pooled, and sorted for live macrophages and DC-enriched populations (CD45$^+$CD3$^-$CD19$^-$SiglecF$^-$Ly6G$^-$7AAD$^-$).

Orthotopic KP-2 tumors were taken from p21$^{CE}$ and p21$^{WT}$ mice, and three from each genotype were pooled as one sample and sorted for live CD45$^+$ cells (CD45$^+$7AAD$^-$). Two libraries were created for each genotype.

Sorted cells from each sample were encapsulated into droplets and libraries were prepared using Chromium Single Cell 3′ v3 Reagent kits according to the manufacturer's protocol (10X Genomics). The generated libraries were sequenced by a NovaSeq 6000 sequencing system (Illumina) to an average of 50,000 mean reads per cell. Cellranger mkfastq pipeline (10X Genomics) was used to demultiplex illumine base call files to FASTQ files. Files from the normal pancreas, pancreatic tumors, and orthotopic tumors were demultiplexed with >97% valid barcodes, and >94% q30 reads. YFP sequences were inserted into the mm10 reference (v.3.1.0; 10X Genomics) using the Cellranger Mkref pipeline. Afterwards, fastq files from each sample were processed with Cellranger counts and aligned to the mm10 reference (v.3.1.0, 10X Genomics) or mm10 containing YFP for p21$^{CE}$ orthotopic tumor samples and the generated feature barcode matrix.

Human scRNAseq data were obtained from a publicly available dataset (Peng et al., 2019). FASTQ files were realigned to the human GRCh38 reference and generated feature barcode matrix, including 24 PDAC samples and 11 normal samples. However, only 21 PDAC samples and six normal samples successfully passed the Cellranger count function.

Mouse scRNAseq data (mPDAC GEMM-1) used in Fig. 3, A and B; Fig. 4, L and M; and Fig. S2 F were obtained from a published paper (Hosein et al., 2019). All scRNAseq data generated for this paper are available with accession number of GSE203026.

**Mouse scRNAseq data analysis**
The filtered feature barcode matrix from the normal pancreas, KPC pancreatic tumors, and p21$^{WT}$ orthotopic tumors were loaded into Seurat as Seurat objects (Seurat v.3). For each Seurat object, genes that were expressed in less than three cells and cells that expressed <1,000 or more than 8,000 genes were excluded. Cells with >6% mitochondrial RNA content were also excluded, resulting in 9,821 cells for normal, 6,091 for KPC tumors, and 16,904 for orthotopic tumors. SCTransform with default parameters was used on each individual sample to normalize and scale the expression matrix against the sequence depths and percentages of mitochondrial genes. Cell cycle scores and the corresponding cell cycle phase for each cell were calculated and assigned after SCTransform based on the expression signatures for S and G2/M genes (CellCycleScoring). The differences between the S phase score and G2/M score were regressed-out by SCTransform on individual samples. Variable features were calculated for each sample independently and ranked, based on the number of samples they were independently identified (SelectIntegrationFeatures). The top 3,000 shared variable features were used for multi-set canonical correlation analysis to reduce dimensions and identify projection vectors that defined shared biological states among samples and maximized overall correlations across datasets. Mutual nearest neighbors (pairs of cells, with one from each

dataset) were calculated and identified as "anchors" (FindIntegrationAnchors). Multiple datasets were then integrated based on these calculated "anchors" and guided order trees with default parameters (IntegrateData). Principal component analysis (PCA) was performed on the 3,000 variable genes calculated earlier (function RunPCA). A UMAP dimensional reduction was performed on the scaled matrix using the first 25 PCA components to obtain a two-dimensional representation of cell states. Then, these defined 25 dimensionalities were used to refine the edge weights between any two cells based on Jaccard similarity (FindNeighbors), and were used to cluster cells through FindClusters functions, which implemented shared nearest neighbor modularity optimization with a resolution of 0.3, leading to 21 clusters.

To characterize clusters, the FindAllMarkers function with logfold threshold = 0.25 and minimum 0.25-fold difference and model-based analysis of single-cell transcriptomics (MAST) test were used to identify signatures alone with each cluster. The macrophage/monocytes (clusters 0, 1, 2, 4, 6, 13, and 17) were selected and the top 3,000 variable features were recalculated to recluster to a higher resolution of 1. Macrophages were selected based on clusters with high expressions of known macrophage marker genes, including *Csf1r*, *C1qa*, *C1qb*, and *H2-Aa*, and confirmed by the absence of *Cd3e*, *Ms4a1*, *Krt19*, *Zbtb46*, and *Flt3*, and further confirmed by identifying DEGs associated with potential macrophage clusters, when compared to known macrophage specific marker genes. In Fig. 1 M, we reran SCTransform without regressing-out cell cycle scores to visualize proliferating macrophage clusters. In Fig. 4, K and L, monocyte clusters were removed based on expressions of monocyte markers, *Ly6c2*, *Plac8*, and *Vcan*. Macrophages were then stratified based on p21 expression into p21$^{High}$ (top 10%) and p21$^{Low}$ (bottom 10%), resulting in 219 of p21$^{High}$ vs. 182 of p21$^{Low}$ TAMs in KPC tumor, and 475 of p21$^{High}$ vs. 526 of p21$^{Low}$ TAMs in KP-2 orthotopic tumors. For GSEA comparisons, the log$_2$ (foldchange) of all genes detected with min.pct > 0.1 and past MAST test was used as a ranking metric. GSEA was performed using Gene Ontology (GO) terms, Kyoto Encyclopedia of Genes and Genomes (KEGG) pathways, Reactome, and Molecular Signatures Database (MSigDB) gene sets with Benjamini–Hochberg FDR < 0.05 in ClusterProfiler (Wu et al., 2021). For DEGs between the two groups in each mouse PDAC model, we filtered genes with a Bonferroni-corrected P value <0.05 and fold-change >1.2 or <0.8.

For the mouse dataset (Hosein et al., 2019), the filtered feature barcode matrices, containing KIC, KPC, and KPFC, were processed similarly with major cell types annotated in Fig. 3 B. Macrophages were then selected and stratified based on p21 expressions into p21$^{High}$ (top 10%) and p21$^{Low}$ (bottom 10%), resulting in 263 of p21$^{High}$ TAMs vs. 237 of p21$^{Low}$ TAMs.

For p21$^{CE}$ and p21$^{WT}$ comparisons, the filtered feature barcode matrix was processed similarly, ending with 16,931 cells for p21$^{WT}$ tumors, and 9,519 cells for p21$^{CE}$ tumors. Cell cycle scores and the corresponding cell cycle phase for each cell were calculated and assigned after SCTransform based on the expression signatures for S and G2/M associated genes (CellCycleScoring). The top 3,000 variable genes, 25 dimensionalities, and resolution of 0.3 generated 19 clusters (Fig. S4, A and B), including

16,093 cells for p21$^{CE}$ tumors and 8,996 cells for p21$^{WT}$ tumors. Each population, including macrophages (clusters 1, 3, 5, 12, 15, and 18), monocytes (cluster 2), DCs (clusters 4, 11, 9, and 16), neutrophils (cluster 14), and eosinophils (cluster 0) were subsetted, at 15 dimensionalities and resolutions of 1 to generate Fig. 6 C, Fig. 7 A, and Fig. S4 E. Cell cycle effects were also regressed-out when subsetting on each cell type, except for macrophages. DEGs with minimum percentage >0.1, a Bonferroni-corrected P value <0.05, and fold-change >1.3 or <0.75 were considered significant. The log$_2$ (fold-change) of all genes detected with minimum percentage >0.1 and past MAST tests were used as a ranking metric for GSEA analysis. Gene sets with FDR <0.05 were considered significant.

### Human scRNAseq data analysis

For the human dataset (Peng et al., 2019), cells with >15% mitochondrial genes were retained and cells that expressed <500 genes were excluded. SCTransform with default parameters was used on each individual sample to normalize and scale the expression matrix against sequence depth and percentage of mitochondrial genes. Cell cycle scores and the corresponding cell cycle phase for each cell were calculated and then assigned after SCTransform based on the expression signatures for S and G2/M genes (CellCycleScoring). The differences between S phase scores and G2/M scores were regressed out by SCTransform on individual samples. Variable features were calculated for every sample in the dataset independently and ranked based on the number of samples they were independently identified (SelectIntegrationFeatures). The top 3,000 shared variable features were used for PCA. The calculated PCA embedding of each cell was then used as an input for the soft k-means clustering algorithm. Briefly, through iteration, the algorithm designated the cluster-specific centroids and cell-specific correction factors corresponding to batch effects. The correction factors were used to assign cells into clusters until the assignment was stable (RunHarmony). Afterwards, similar steps were taken; UMAP reduction used the first 20 PCA components and FindClusters with a resolution of 0.3, leading to 12 clusters (Fig. 3 D). Immune cell clusters (3, 4, 9, and 10) were reclustered, reintegrated (RunHarmony), and UMAP reduction was used with a resolution of 0.5 to generate 11 clusters. The clusters were further grouped into NKT cells, Tregs, T cells, myeloid cells, and B cells in Fig. 1, K and L.

### The mpIHC

Mouse tissues were fixed in 10% formalin for 24 h and embedded in paraffin after graded ethanol dehydration. Embedded tissues were sectioned into 6-μm sections and loaded into BOND RXm (Leica Biosystems) for a series of staining including F4/80, p21, PDPN, Ki67, and CK19. Based on antibody host species, default manufacturer protocols were used (IntenseR and Polymer Refine), containing antigen-retrieval with citrate buffer, goat serum and peroxide block, primary antibody incubation, post-primary incubation, and chromogenically visualized with an AEC substrate (Abcam). Between each two cycles of staining, the slides were manually stained for hemoxylin and eosin, and then scanned by Axio Scan.Z1 (Zeiss). The slides were then destained by a

gradient of ethanol plus a 2% hydrochloride wash and blocked with extra avidin/biotin (Vector Laboratories) and a Fab fragment block (Jackson Laboratory).

Images of the same specimen but different stains were cropped into multiple segments by Zen software (Zeiss). Each segment was then deconvoluted (Deconvolution, v.1.0.4; Indica Labs) for individual staining and fused using HALO software (Zeiss) with the default manufacturer's settings. Markers of interest were pseudo-colored and quantified through the High plex FL, v.4.0.3 algorithm (Indica Labs).

### Statistical analysis

All statistical analyses were performed using GraphPad Prism software v.8, with final input from a biostatistics core expert at Washington University. All data are representative of at least two independent experiments, unless specifically noted. Sample size was pre-calculated to satisfy power-requirements (with >85% confidence) in most experiments and is specified in the figure legends wherever applicable. Data are shown as mean ± SEM, unless otherwise noted. Normal distribution of data was assessed using the D'Agostino–Pearson omnibus normality test in Prism. Statistical tests such as unpaired parametric Student's $t$ test, ANOVA analysis (Bonferroni multiple comparison) or unpaired non-parametric Mann–Whitney U-test were used appropriately based on normality of data. For proximity analyses, the non-parametric Kolmogorov–Smirnov test was used to distinguish differences in frequency distributions. P < 0.05 was considered statistically significant for all studies.

### Online supplemental material

Fig. S1 identifies cell types in human CyTOF analyses and demonstrates workflow for flow cytometry and scRNAseq analyses of murine pancreatic tissues. Fig. S2 supports siRNA knockdown of p21 in BMDMs in vitro and shows p21 expression in TAMs and its connection to cell cycle states, as well as its regulation by fibroblast-derived CSF1 and chemotherapeutics. Representative images used to evaluate mpIHC staining of murine PDAC tissues are also included. Fig. S3 demonstrates flow cytometry and complete blood count analyses of the immune compositions in non-tumor-bearing p21$^{CE}$ and p21$^{WT}$ mice, and in tumor-bearing p21$^{CE}$ and p21$^{WT}$ mice, as well as phenotypic characterization of TAMs. Fig. S4 identifies major clusters in scRNAseq analyses performed on tumor-bearing p21$^{CE}$ and p21$^{WT}$ mice. It also provides data for macrophage depletion experiment and in vitro macrophage suppression of CD8 T cell function assays. Fig. S5 shows the GSEA results when comparing TAMs from p21$^{CE}$ to p21$^{WT}$ and additional analyses of macrophage subsets. Table S1 lists the top 50 DEGs in p21-deprived BMDMs cultured in tumor-conditioned medium. Table S2 lists all siRNA sequences, antibodies, primers, organisms and strains, software and algorithms, chemicals and recombinant proteins, and commercial assays used in this study.

## References

Abram, C.L., G.L. Roberge, Y. Hu, and C.A. Lowell. 2014. Comparative analysis of the efficiency and specificity of myeloid-Cre deleting strains using ROSA-EYFP reporter mice. *J. Immunol. Methods.* 408:89–100. https://doi.org/10.1016/j.jim.2014.05.009

Amano, S.U., J.L. Cohen, P. Vangala, M. Tencerova, S.M. Nicoloro, J.C. Yawe, Y. Shen, M.P. Czech, and M. Aouadi. 2014. Local proliferation of macrophages contributes to obesity-associated adipose tissue inflammation. *Cell Metab.* 19:162–171. https://doi.org/10.1016/j.cmet.2013.11.017

Balkwill, F. 2006. TNF-alpha in promotion and progression of cancer. *Cancer Metastasis Rev.* 25:409–416. https://doi.org/10.1007/s10555-006-9005-3

Borgoni, S., A. Iannello, S. Cutrupi, P. Allavena, M. D'Incalci, F. Novelli, and P. Cappello. 2017. Depletion of tumor-associated macrophages switches the epigenetic profile of pancreatic cancer infiltrating T cells and restores their anti-tumor phenotype. *OncoImmunology.* 7:e1393596. https://doi.org/10.1080/2162402X.2017.1393596

Bottazzi, B., E. Erba, N. Nobili, F. Fazioli, A. Rambaldi, and A. Mantovani. 1990. A paracrine circuit in the regulation of the proliferation of macrophages infiltrating murine sarcomas. *J. Immunol.* 144:2409–2412. https://doi.org/10.4049/jimmunol.144.6.2409

Brugarolas, J., K. Moberg, S.D. Boyd, Y. Taya, T. Jacks, and J.A. Lees. 1999. Inhibition of cyclin-dependent kinase 2 by p21 is necessary for retinoblastoma protein-mediated G1 arrest after γ-irradiation. *Proc. Natl. Acad. Sci. USA.* 96:1002–1007. https://doi.org/10.1073/pnas.96.3.1002

Candido, J.B., J.P. Morton, P. Bailey, A.D. Campbell, S.A. Karim, T. Jamieson, L. Lapienyte, A. Gopinathan, W. Clark, E.J. McGhee, et al. 2018. CSF1R+ macrophages sustain pancreatic tumor growth through T cell suppression and maintenance of key gene programs that define the squamous subtype. *Cell Rep.* 23:1448–1460. https://doi.org/10.1016/j.celrep.2018.03.131

Cannarile, M.A., M. Weisser, W. Jacob, A.-M. Jegg, C.H. Ries, and D. Rüttinger. 2017. Colony-stimulating factor 1 receptor (CSF1R) inhibitors in cancer therapy. *J. Immunother. Cancer.* 5:53. https://doi.org/10.1186/s40425-017-0257-y

Cassetta, L., and J.W. Pollard. 2018. Targeting macrophages: Therapeutic approaches in cancer. *Nat. Rev. Drug Discov.* 17:887–904. https://doi.org/10.1038/nrd.2018.169

Castro-Dopico, T., and M.R. Clatworthy. 2019. IgG and Fcγ receptors in intestinal immunity and inflammation. *Front. Immunol.* 10:805. https://doi.org/10.3389/fimmu.2019.00805

Cazzalini, O., A.I. Scovassi, M. Savio, L.A. Stivala, and E. Prosperi. 2010. Multiple roles of the cell cycle inhibitor p21(CDKN1A) in the DNA damage response. *Mutat. Res.* 704:12–20. https://doi.org/10.1016/j.mrrev.2010.01.009

Clausen, B.E., C. Burkhardt, W. Reith, R. Renkawitz, and I. Förster. 1999. Conditional gene targeting in macrophages and granulocytes using LysMcre mice. *Transgenic Res.* 8:265–277. https://doi.org/10.1023/a:1008942828960

Coveler, A.L., D.L. Bajor, A. Masood, E. Yilmaz, A.F. Shields, M.M. Javle, R.K. Paluri, G.M. Vaccaro, M. Zalupski, J.E. Grilley-Olson, et al. 2020. Phase I study of SEA-CD40, gemcitabine, nab-paclitaxel, and pembrolizumab in patients with metastatic pancreatic ductal adenocarcinoma (PDAC). *J. Clin. Oncol.* 38:TPS4671. https://doi.org/10.1200/JCO.2020.38.15_suppl.TPS4671

Davies, L.C., M. Rosas, P.J. Smith, D.J. Fraser, S.A. Jones, and P.R. Taylor. 2011. A quantifiable proliferative burst of tissue macrophages restores homeostatic macrophage populations after acute inflammation. *Eur. J. Immunol.* 41:2155–2164. https://doi.org/10.1002/eji.201141817

DeNardo, D.G., and B. Ruffell. 2019. Macrophages as regulators of tumour immunity and immunotherapy. *Nat. Rev. Immunol.* 19:369–382. https://doi.org/10.1038/s41577-019-0127-6

Deng, C., P. Zhang, J.W. Harper, S.J. Elledge, and P. Leder. 1995. Mice lacking p21CIP1/WAF1 undergo normal development, but are defective in G1 checkpoint control. *Cell.* 82:675–684. https://doi.org/10.1016/0092-8674(95)90039-x

Doedens, A.L., C. Stockmann, M.P. Rubinstein, D. Liao, N. Zhang, D.G. DeNardo, L.M. Coussens, M. Karin, A.W. Goldrath, and R.S. Johnson. 2010. Macrophage expression of hypoxia-inducible factor-1 alpha suppresses T-cell function and promotes tumor progression. *Cancer Res.* 70:7465–7475. https://doi.org/10.1158/0008-5472.CAN-10-1439

Dutto, I., M. Tillhon, O. Cazzalini, L.A. Stivala, and E. Prosperi. 2015. Biology of the cell cycle inhibitor p21(CDKN1A): Molecular mechanisms and relevance in chemical toxicology. *Arch. Toxicol.* 89:155–178. https://doi.org/10.1007/s00204-014-1430-4

Elyada, E., M. Bolisetty, P. Laise, W.F. Flynn, E.T. Courtois, R.A. Burkhart, J.A. Teinor, P. Belleau, G. Biffi, M.S. Lucito, et al. 2019. Cross-species single-cell analysis of pancreatic ductal adenocarcinoma reveals antigen-presenting cancer-associated fibroblasts. *Cancer Discov.* 9:1102–1123. https://doi.org/10.1158/2159-8290.CD-19-0094

Finck, R., E.F. Simonds, A. Jager, S. Krishnaswamy, K. Sachs, W. Fantl, D. Pe'er, G.P. Nolan, and S.C. Bendall. 2013. Normalization of mass cytometry data with bead standards. *Cytometry A.* 83:483–494. https://doi.org/10.1002/cyto.a.22271

Franklin, R.A., W. Liao, A. Sarkar, M.V. Kim, M.R. Bivona, K. Liu, E.G. Pamer, and M.O. Li. 2014. The cellular and molecular origin of tumor-associated macrophages. *Science.* 344:921–925. https://doi.org/10.1126/science.1252510

Gardner, A., and B. Ruffell. 2016. Dendritic cells and cancer immunity. *Trends Immunol.* 37:855–865. https://doi.org/10.1016/j.it.2016.09.006

Ginhoux, F., and M. Guilliams. 2016. Tissue-resident macrophage ontogeny and homeostasis. *Immunity.* 44:439–449. https://doi.org/10.1016/j.immuni.2016.02.024

Hao, N.-B., M.-H. Lü, Y.-H. Fan, Y.-L. Cao, Z.-R. Zhang, and S.-M. Yang. 2012. Macrophages in tumor microenvironments and the progression of tumors. *Clin. Dev. Immunol.* 2012:948098. https://doi.org/10.1155/2012/948098

Hashimoto, D., A. Chow, C. Noizat, P. Teo, M.B. Beasley, M. Leboeuf, C.D. Becker, P. See, J. Price, D. Lucas, et al. 2013. Tissue-resident macrophages self-maintain locally throughout adult life with minimal contribution from circulating monocytes. *Immunity.* 38:792–804. https://doi.org/10.1016/j.immuni.2013.04.004

Hervas-Stubbs, S., J.L. Perez-Gracia, A. Rouzaut, M.F. Sanmamed, A. Le Bon, and I. Melero. 2011. Direct effects of type I interferons on cells of the immune system. *Clin. Cancer Res.* 17:2619–2627. https://doi.org/10.1158/1078-0432.CCR-10-1114

Hingorani, S.R., E.F. Petricoin III, A. Maitra, V. Rajapakse, C. King, M.A. Jacobetz, S. Ross, T.P. Conrads, T.D. Veenstra, B.A. Hitt, et al. 2003. Preinvasive and invasive ductal pancreatic cancer and its early detection in the mouse. *Cancer Cell.* 4:437–450. https://doi.org/10.1016/S1535-6108(03)00309-X

Hingorani, S.R., L. Wang, A.S. Multani, C. Combs, T.B. Deramaudt, R.H. Hruban, A.K. Rustgi, S. Chang, and D.A. Tuveson. 2005. Trp53R172H and KrasG12D cooperate to promote chromosomal instability and

widely metastatic pancreatic ductal adenocarcinoma in mice. *Cancer Cell*. 7:469–483. https://doi.org/10.1016/j.ccr.2005.04.023

Hosein, A.N., H. Huang, Z. Wang, K. Parmar, W. Du, J. Huang, A. Maitra, E. Olson, U. Verma, and R.A. Brekken. 2019. Cellular heterogeneity during mouse pancreatic ductal adenocarcinoma progression at single-cell resolution. *JCI Insight*. 5:e129212. https://doi.org/10.1172/jci.insight .129212

Hsu, C.-H., S.J. Altschuler, and L.F. Wu. 2019. Patterns of early p21 dynamics determine proliferation-senescence cell fate after chemotherapy. *Cell*. 178:361–373.e12. https://doi.org/10.1016/j.cell.2019.05.041

Ino, Y., R. Yamazaki-Itoh, K. Shimada, M. Iwasaki, T. Kosuge, Y. Kanai, and N. Hiraoka. 2013. Immune cell infiltration as an indicator of the immune microenvironment of pancreatic cancer. *Br. J. Cancer*. 108:914–923. https://doi.org/10.1038/bjc.2013.32

Jenkins, S.J., D. Ruckerl, P.C. Cook, L.H. Jones, F.D. Finkelman, N. van Rooijen, A.S. MacDonald, and J.E. Allen. 2011. Local macrophage proliferation, rather than recruitment from the blood, is a signature of TH2 inflammation. *Science*. 332:1284–1288. https://doi.org/10.1126/science.1204351

Jenkins, S.J., D. Ruckerl, G.D. Thomas, J.P. Hewitson, S. Duncan, F. Brombacher, R.M. Maizels, D.A. Hume, and J.E. Allen. 2013. IL-4 directly signals tissue-resident macrophages to proliferate beyond homeostatic levels controlled by CSF-1. *J. Exp. Med*. 210:2477–2491. https://doi.org/10 .1084/jem.20121999

Jiang, H., S. Hegde, B.L. Knolhoff, Y. Zhu, J.M. Herndon, M.A. Meyer, T.M. Nywening, W.G. Hawkins, I.M. Shapiro, D.T. Weaver, et al. 2016. Targeting focal adhesion kinase renders pancreatic cancers responsive to checkpoint immunotherapy. *Nat. Med*. 22:851–860. https://doi.org/10 .1038/nm.4123

Kaplan, D.H. 2017. Ontogeny and function of murine epidermal Langerhans cells. *Nat. Immunol*. 18:1068–1075. https://doi.org/10.1038/ni.3815

Karmaus, P.W.F., A.A. Herrada, C. Guy, G. Neale, Y. Dhungana, L. Long, P. Vogel, J. Avila, C.B. Clish, and H. Chi. 2017. Critical roles of mTORC1 signaling and metabolic reprogramming for M-CSF-mediated myelopoiesis. *J. Exp. Med*. 214:2629–2647. https://doi.org/10.1084/jem.20161855

Kim, M.P., D.B. Evans, H. Wang, J.L. Abbruzzese, J.B. Fleming, and G.E. Gallick. 2009. Generation of orthotopic and heterotopic human pancreatic cancer xenografts in immunodeficient mice. *Nat. Protoc*. 4: 1670–1680. https://doi.org/10.1038/nprot.2009.171

Kitajima, S., R. Thummalapalli, and D.A. Barbie. 2016. Inflammation as a driver and vulnerability of KRAS mediated oncogenesis. *Semin. Cell Dev. Biol*. 58:127–135. https://doi.org/10.1016/j.semcdb.2016.06.009

Korsunsky, I., N. Millard, J. Fan, K. Slowikowski, F. Zhang, K. Wei, Y. Baglaenko, M. Brenner, P.-R. Loh, and S. Raychaudhuri. 2019. Fast, sensitive and accurate integration of single-cell data with Harmony. *Nat. Methods*. 16:1289–1296. https://doi.org/10.1038/s41592-019-0619-0

Koucký, V., J. Bouček, and A. Fialová. 2019. Immunology of plasmacytoid dendritic cells in solid tumors: A brief review. *Cancers*. 11:470. https:// doi.org/10.3390/cancers11040470

Kumar, V., L. Donthireddy, D. Marvel, T. Condamine, F. Wang, S. Lavilla-Alonso, A. Hashimoto, P. Vonteddu, R. Behera, M.A. Goins, et al. 2017. Cancer-associated fibroblasts neutralize the anti-tumor effect of CSF1 receptor blockade by inducing PMN-MDSC infiltration of tumors. *Cancer Cell*. 32:654–668.e5. https://doi.org/10.1016/j.ccell.2017.10.005

Lee, A.W., S. Nambirajan, and J.G. Moffat. 1999. CSF-1 activates MAPK-dependent and p53-independent pathways to induce growth arrest of hormone-dependent human breast cancer cells. *Oncogene*. 18:7477–7494. https://doi.org/10.1038/sj.onc.1203123

Lee, J.W., C.A. Komar, F. Bengsch, K. Graham, and G.L. Beatty. 2016. Genetically engineered mouse models of pancreatic cancer: The KPC model (LSL-Kras(G12D/+); LSL-Trp53(R172H/+); Pdx-1-Cre), its variants, and their application in immuno-oncology drug discovery. *Curr. Protoc. Pharmacol*. 73:14.39.1–14.39.20. https://doi.org/10.1002/cpph.2

Levine, J.H., E.F. Simonds, S.C. Bendall, K.L. Davis, A.D. Amir, M.D. Tadmor, O. Litvin, H.G. Fienberg, A. Jager, E.R. Zunder, et al. 2015. Data-driven phenotypic dissection of AML reveals progenitor-like cells that correlate with prognosis. *Cell*. 162:184–197. https://doi.org/10.1016/j.cell.2015.05.047

Lin, K.-Y., D. Lu, C.-F. Hung, S. Peng, L. Huang, C. Jie, F. Murillo, J. Rowley, Y.-C. Tsai, L. He, et al. 2007. Ectopic expression of vascular cell adhesion molecule-1 as a new mechanism for tumor immune evasion. *Cancer Res*. 67:1832–1841. https://doi.org/10.1158/0008-5472.CAN-06-3014

Liu, L., Y. Lu, J. Martinez, Y. Bi, G. Lian, T. Wang, S. Milasta, J. Wang, M. Yang, G. Liu, et al. 2016. Proinflammatory signal suppresses proliferation and shifts macrophage metabolism from Myc-dependent to HIF1α-dependent. *Proc. Natl. Acad. Sci. USA*. 113:1564–1569. https://doi.org/10.1073/pnas .1518000113

Lun, A.T.L., A.C. Richard, and J.C. Marioni. 2017. Testing for differential abundance in mass cytometry data. *Nat. Methods*. 14:707–709. https://doi .org/10.1038/nmeth.4295

Marchant, A., C. Bruyns, P. Vandenabeele, M. Ducarme, C. Gérard, A. Delvaux, D. De Groote, D. Abramowicz, T. Velu, and M. Goldman. 1994. Interleukin-10 controls interferon-gamma and tumor necrosis factor production during experimental endotoxemia. *Eur. J. Immunol*. 24: 1167–1171. https://doi.org/10.1002/eji.1830240524

Martin, C., D. Ohayon, M. Alkan, J. Mocek, M. Pederzoli-Ribeil, C. Candalh, G. Thevenot, A. Millet, N. Tamassia, M.A. Cassatella, et al. 2016. Neutrophil-expressed p21/waf1 favors inflammation resolution in *Pseudomonas aeruginosa* infection. *Am. J. Respir. Cell Mol. Biol*. 54: 740–750. https://doi.org/10.1165/rcmb.2015-0047OC

Matsushime, H., M.F. Roussel, R.A. Ashmun, and C.J. Sherr. 1991. Colony-stimulating factor 1 regulates novel cyclins during the G1 phase of the cell cycle. *Cell*. 65:701–713. https://doi.org/10.1016/0092-8674(91) 90101-4

Mavers, M., C.M. Cuda, A.V. Misharin, A.K. Gierut, H. Agrawal, E. Weber, D.V. Novack, G.K. Haines III, D. Balomenos, and H. Perlman. 2012. Cyclin-dependent kinase inhibitor p21, via its C-terminal domain, is essential for resolution of murine inflammatory arthritis. *Arthritis Rheum*. 64:141–152. https://doi.org/10.1002/art.33311

McInnes, L., J. Healy, and J. Melville. 2020. UMAP: Uniform manifold approximation and projection for dimension reduction. *arXiv*. https://doi .org/10.48550/arXiv.1802.03426

Merad, M., P. Sathe, J. Helft, J. Miller, and A. Mortha. 2013. The dendritic cell lineage: Ontogeny and function of dendritic cells and their subsets in the steady state and the inflamed setting. *Annu. Rev. Immunol*. 31: 563–604. https://doi.org/10.1146/annurev-immunol-020711-074950

Mitchem, J.B., D.J. Brennan, B.L. Knolhoff, B.A. Belt, Y. Zhu, D.E. Sanford, L. Belaygorod, D. Carpenter, L. Collins, D. Piwnica-Worms, et al. 2013. Targeting tumor-infiltrating macrophages decreases tumor-initiating cells, relieves immunosuppression, and improves chemotherapeutic responses. *Cancer Res*. 73:1128–1141. https://doi.org/10.1158/0008-5472 .CAN-12-2731

Müller, E., P.F. Christopoulos, S. Halder, A. Lunde, K. Beraki, M. Speth, I. Øynebråten, and A. Corthay. 2017. Toll-like receptor ligands and interferon-γ synergize for induction of antitumor M1 macrophages. *Front. Immunol*. 8:1383. https://doi.org/10.3389/fimmu.2017.01383

Nowicka, M., C. Krieg, H.L. Crowell, L.M. Weber, F.J. Hartmann, S. Guglietta, B. Becher, M.P. Levesque, and M.D. Robinson. 2017. CyTOF workflow: Differential discovery in high-throughput high-dimensional cytometry datasets. *F1000 Res*. 6:748. https://doi.org/10.12688/f1000research.11622.3

Noy, R., and J.W. Pollard. 2014. Tumor-associated macrophages: From mechanisms to therapy. *Immunity*. 41:49–61. https://doi.org/10.1016/j .immuni.2014.06.010

Peng, J., B.-F. Sun, C.-Y. Chen, J.-Y. Zhou, Y.-S. Chen, H. Chen, L. Liu, D. Huang, J. Jiang, G.-S. Cui, et al. 2019. Single-cell RNA-seq highlights intra-tumoral heterogeneity and malignant progression in pancreatic ductal adenocarcinoma. *Cell Res*. 29:725–738. https://doi.org/10.1038/ s41422-019-0195-y

Poh, A.R., and M. Ernst. 2018. Targeting macrophages in cancer: From bench to bedside. *Front. Oncol*. 8:49. https://doi.org/10.3389/fonc.2018.00049

Rackov, G., E. Hernández-Jiménez, R. Shokri, L. Carmona-Rodríguez, S. Mañes, M. Álvarez-Mon, E. López-Collazo, C. Martínez-A, and D. Balomenos. 2016. p21 mediates macrophage reprogramming through regulation of p50-p50 NF-κB and IFN-β. *J. Clin. Invest*. 126:3089–3103. https://doi.org/10.1172/JCI83404

Ruffell, B., and L.M. Coussens. 2015. Macrophages and therapeutic resistance in cancer. *Cancer Cell*. 27:462–472. https://doi.org/10.1016/j.ccell.2015 .02.015

Salomon, B.L., M. Leclerc, J. Tosello, E. Ronin, E. Piaggio, and J.L. Cohen. 2018. Tumor necrosis factor α and regulatory T cells in oncoimmunology. *Front. Immunol*. 9:444. https://doi.org/10.3389/fimmu.2018.00444

Samain, R., A. Brunel, T. Douché, M. Fanjul, S. Cassant-Sourdy, J. Rochotte, J. Cros, C. Neuzillet, J. Raffenne, C. Duluc, et al. 2021. Pharmacologic normalization of pancreatic cancer-associated fibroblast secretome impairs prometastatic cross-talk with macrophages. *Cell. Mol. Gastroenterol. Hepatol*. 11:1405–1436. https://doi.org/10.1016/j .jcmgh.2021.01.008

Scatizzi, J.C., J. Hutcheson, E. Bickel, J.M. Woods, K. Klosowska, T.L. Moore, G.K. Haines III, and H. Perlman. 2006. p21Cip1 is required for the development of monocytes and their response to serum transfer-induced arthritis. *Am. J. Pathol*. 168:1531–1541. https://doi.org/10.2353/ajpath .2006.050555

Schnittert, J., R. Bansal, and J. Prakash. 2019. Targeting pancreatic stellate cells in cancer. *Trends Cancer*. 5:128–142. https://doi.org/10.1016/j.trecan.2019.01.001

Seleznik, G.M., T. Reding, L. Peter, A. Gupta, S.G. Steiner, S. Sonda, C.S. Verbeke, E. Dejardin, I. Khatkov, S. Segerer, et al. 2018. Development of autoimmune pancreatitis is independent of CDKN1A/p21-mediated pancreatic inflammation. *Gut*. 67:1663–1673. https://doi.org/10.1136/gutjnl-2016-313458

Sewing, A., B. Wiseman, A.C. Lloyd, and H. Land. 1997. High-intensity Raf signal causes cell cycle arrest mediated by p21Cip1. *Mol. Cell. Biol.* 17:5588–5597. https://doi.org/10.1128/MCB.17.9.5588

Stuart, T., A. Butler, P. Hoffman, C. Hafemeister, E. Papalexi, W.M. Mauck, 3rd, Y. Hao, M. Stoeckius, P. Smibert, and R. Satija. 2019. Comprehensive Integration of Single-Cell Data. *Cell*. 177:1888–1902. https://doi.org/10.1016/j.cell.2019.05.031

Tang, J., M.E. Lobatto, L. Hassing, S. van der Staay, S.M. van Rijs, C. Calcagno, M.S. Braza, S. Baxter, F. Fay, B.L. Sanchez-Gaytan, et al. 2015. Inhibiting macrophage proliferation suppresses atherosclerotic plaque inflammation. *Sci. Adv.* 1:e1400223. https://doi.org/10.1126/sciadv.1400223

Tirosh, I., B. Izar, S.M. Prakadan, M.H. Wadsworth II, D. Treacy, J.J. Trombetta, A. Rotem, C. Rodman, C. Lian, G. Murphy, et al. 2016. Dissecting the multicellular ecosystem of metastatic melanoma by single-cell RNA-seq. *Science*. 352:189–196. https://doi.org/10.1126/science.aad0501

Trakala, M., C.F. Arias, M.I. García, M.C. Moreno-Ortiz, K. Tsilingiri, P.J. Fernández, M. Mellado, M.T. Díaz-Meco, J. Moscat, M. Serrano, et al. 2009. Regulation of macrophage activation and septic shock susceptibility via p21(WAF1/CIP1). *Eur. J. Immunol.* 39:810–819. https://doi.org/10.1002/eji.200838676

Tymoszuk, P., H. Evens, V. Marzola, K. Wachowicz, M.-H. Wasmer, S. Datta, E. Müller-Holzner, H. Fiegl, G. Böck, N. van Rooijen, et al. 2014. In situ proliferation contributes to accumulation of tumor-associated macrophages in spontaneous mammary tumors. *Eur. J. Immunol.* 44:2247–2262. https://doi.org/10.1002/eji.201344304

Van Gassen, N., E. Van Overmeire, G. Leuckx, Y. Heremans, S. De Groef, Y. Cai, Y. Elkrim, C. Gysemans, B. Stijlemans, M. Van de Casteele, et al. 2015. Macrophage dynamics are regulated by local macrophage proliferation and monocyte recruitment in injured pancreas. *Eur. J. Immunol.* 45:1482–1493. https://doi.org/10.1002/eji.201445013

Waghray, M., M. Yalamanchili, M.P. di Magliano, and D.M. Simeone. 2013. Deciphering the role of stroma in pancreatic cancer. *Curr. Opin. Gastroenterol.* 29:537–543. https://doi.org/10.1097/MOG.0b013e328363affe

Weber, L.M., M. Nowicka, C. Soneson, and M.D. Robinson. 2019. diffcyt: Differential discovery in high-dimensional cytometry via high-resolution clustering. *Commun. Biol.* 2:183. https://doi.org/10.1038/s42003-019-0415-5

Wu, T., E. Hu, S. Xu, M. Chen, P. Guo, Z. Dai, T. Feng, L. Zhou, W. Tang, L. Zhan, et al. 2021. clusterProfiler 4.0: A universal enrichment tool for interpreting omics data. *Innovation*. 2:100141. https://doi.org/10.1016/j.xinn.2021.100141

Xaus, J., M. Comalada, A.F. Valledor, J. Lloberas, F. López-Soriano, J.M. Argilés, C. Bogdan, and A. Celada. 2000. LPS induces apoptosis in macrophages mostly through the autocrine production of TNF-α. *Blood*. 95:3823–3831. https://doi.org/10.1182/blood.V95.12.3823

Xiang, X., J. Wang, D. Lu, and X. Xu. 2021. Targeting tumor-associated macrophages to synergize tumor immunotherapy. *Signal Transduct. Target. Ther.* 6:75. https://doi.org/10.1038/s41392-021-00484-9

Yang, H.W., M. Chung, T. Kudo, and T. Meyer. 2017. Competing memories of mitogen and p53 signalling control cell-cycle entry. *Nature*. 549:404–408. https://doi.org/10.1038/nature23880

Yao, H., S.-R. Yang, I. Edirisinghe, S. Rajendrasozhan, S. Caito, D. Adenuga, M.A. O'Reilly, and I. Rahman. 2008. Disruption of p21 attenuates lung inflammation induced by cigarette smoke, LPS, and fMLP in mice. *Am. J. Respir. Cell Mol. Biol.* 39:7–18. https://doi.org/10.1165/rcmb.2007-0342OC

Zheng, W., and R.A. Flavell. 1997. The transcription factor GATA-3 is necessary and sufficient for Th2 cytokine gene expression in CD4 T cells. *Cell*. 89:587–596. https://doi.org/10.1016/S0092-8674(00)80240-8

Zhu, Y., J.M. Herndon, D.K. Sojka, K.-W. Kim, B.L. Knolhoff, C. Zuo, D.R. Cullinan, J. Luo, A.R. Bearden, K.J. Lavine, et al. 2017. Tissue-resident macrophages in pancreatic ductal adenocarcinoma originate from embryonic hematopoiesis and promote tumor progression. *Immunity*. 47:323–338.e6. https://doi.org/10.1016/j.immuni.2017.07.014

Zhu, Y., B.L. Knolhoff, M.A. Meyer, T.M. Nywening, B.L. West, J. Luo, A. Wang-Gillam, S.P. Goedegebuure, D.C. Linehan, and D.G. DeNardo. 2014. CSF1/CSF1R blockade reprograms tumor-infiltrating macrophages and improves response to T-cell checkpoint immunotherapy in pancreatic cancer models. *Cancer Res.* 74:5057–5069. https://doi.org/10.1158/0008-5472.CAN-13-3723

Zunder, E.R., R. Finck, G.K. Behbehani, A.D. Amir, S. Krishnaswamy, V.D. Gonzalez, C.G. Lorang, Z. Bjornson, M.H. Spitzer, B. Bodenmiller, et al. 2015. Palladium-based mass tag cell barcoding with a doublet-filtering scheme and single-cell deconvolution algorithm. *Nat. Protoc.* 10:316–333. https://doi.org/10.1038/nprot.2015.020
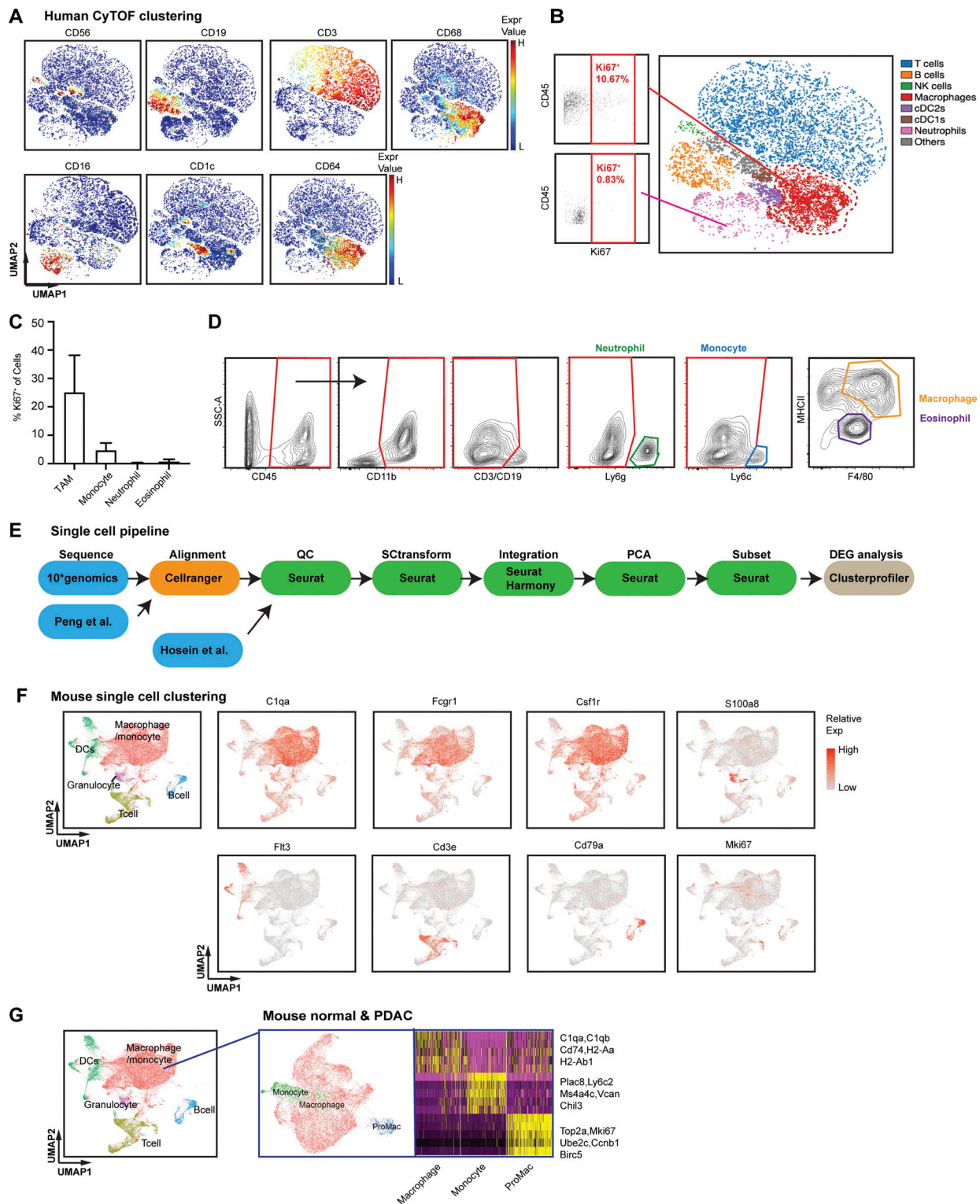
# Supplemental material

Figure S1. **Tumor-infiltrating macrophages are highly proliferative in PDAC. (A)** Representative t-SNE plots of CyTOF analysis of human PDAC samples, displaying markers used for identifying major cell types, CD56+ for natural killer cells, CD19+CD3+ for T cells, CD16+ for neutrophils, CD68+CD64+CD14+ for macrophages, CD1c+ for cDC2, and CD141+ for cDC1 cells; $n$ = 9 PDAC patients. **(B)** Representative Ki67+ gating in macrophage and neutrophil clusters. **(C)** Bar graph displaying percentage of Ki67+ cells in TAMs, monocytes, neutrophils, and eosinophils from B6 mice bearing orthotopic KPC tumor. **(D)** Representative flow cytometry plots showing the gating strategy to identify macrophages, monocytes, neutrophils, and eosinophil in orthotopic KP-2, KPC tumors. **(E)** Schematic of the scRNAseq analysis pipeline. Details of each step for the specific dataset are listed in the Materials and methods. **(F)** UMAP dimensionality reduction plot of integrated sorted CD45+ cells from the murine normal pancreas and pancreatic tissues from KPC PDACs and KP-2 orthotopic PDACs with cell type annotations and cell cycle regression. **(G)** UMAP plot of reclustered macrophages/monocytes in F without cell cycle regression with a heat map displaying corresponding gene signatures.
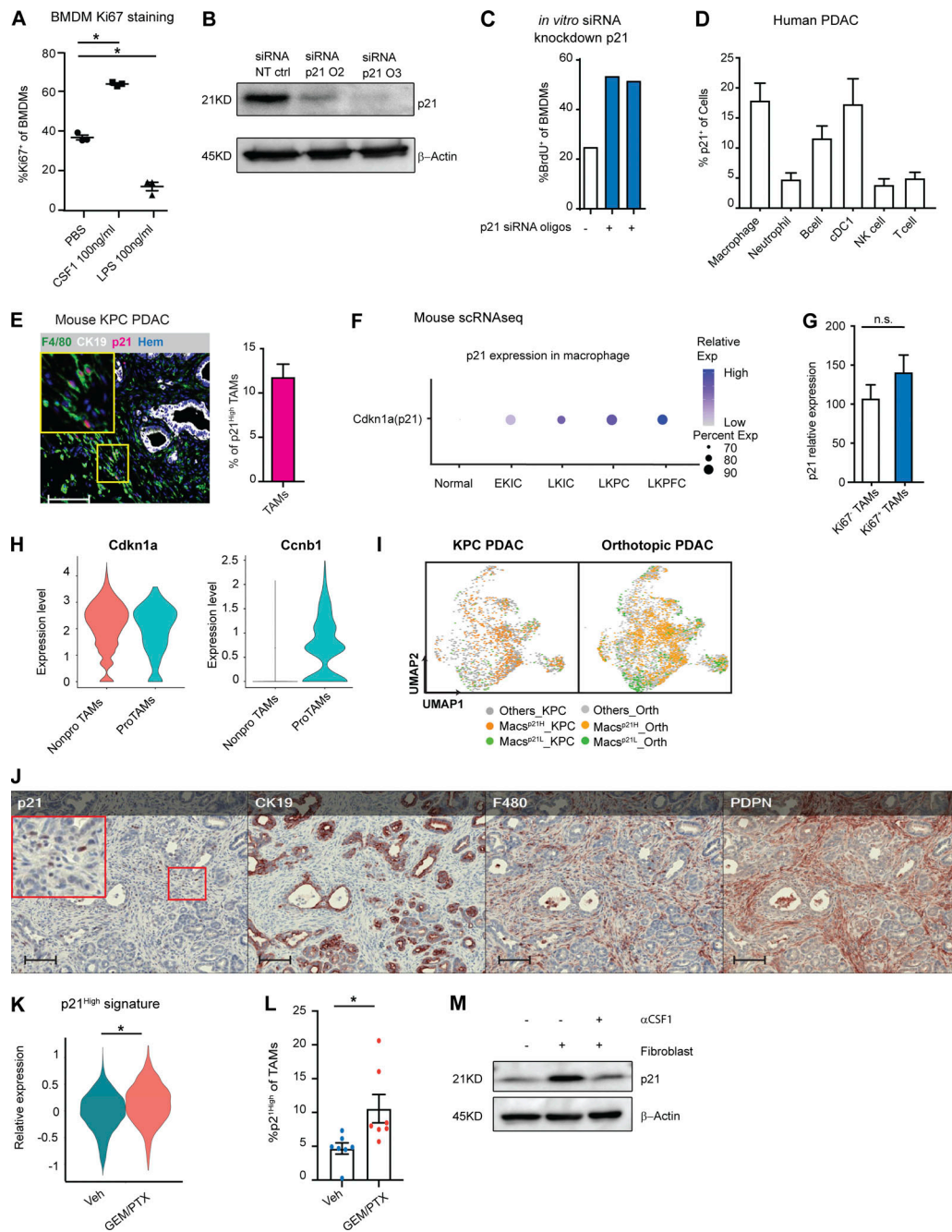
Figure S2. **The p21-expressing TAMs have a distinct phenotype, and p21 expression could be induced by chemotherapy. (A)** Dot plot displaying the percentage of Ki67+ BMDMs after CSF1 or LPS treatment for 24 h; n = 3/group. **(B)** Immunoblot showing expression of p21 in BMDMs after treatment with non-targeting siRNA or siRNA targeting for p21 in the presence of CSF1 for 24 h. Experiments were repeated in more than three independent repeats, and included tumor-conditioned medium treatment or were cultured with fibroblasts in the transwell assays. **(C)** Bar plot displaying quantification of BrdU+ BMDMs in B. The BrdU was pulsed for 20 h. The experiments were repeated three times with three different siRNA oligonucleotides. **(D)** Bar plot showing percentage of p21+ in different immune populations from human PDAC tumors identified in Fig. S1 A. **(E)** Representative image of mpIHC for F4/80+ macrophages, CK19+ tumor cells, and p21+ cells with quantification of p21+ macrophages from KPC PDACs; n = 8. **(F)** Dot plot showing Cdkn1a (p21) gene expressions in the normal pancreas and pancreatic tissues from EKIC, LKIC, LKPC, and LKPFC GEMMs (Hosein et al., 2019). **(G)** Bar plot showing the expression levels of p21 in Ki67+ and Ki67− TAMs identified in Fig. S1 B; n = 9. **(H)** Violin plot of the expressions of p21 and Ccnb1 in non-proliferating and proliferating macrophages in the mouse scRNAseq dataset from the KPC, orthotopic KP-2, and normal pancreas in Fig. 1 M. **(I)** UMAP displaying p21High and p21Low macrophages in KPC PDAC tumors and orthotopic KP-2 tumors. **(J)** Representative mpIHC images of KPC mouse PDACs displaying p21, CK19, F4/80, and Pdpn staining; n = 8. Scale bars, 100 μm. **(K)** Violin plot displaying the expressions of p21High signature scores, identified in Fig. 4 M, in TAMs from KPC mice 24 h after GEM/PTX or dimethyl sulfoxide treatment. **(L)** Bar plot showing percentage of p21High TAMs in KPC GEMM PDAC after DMSO or GEM/PTX treatments. **(M)** Immunoblot showing expression of p21 in BMDMs in the transwell assay with fibroblast with or without addition of αCSF1 for 24 h. All graphs are expressed as the mean ± SEM. *, P < 0.05. All in vitro assays were consistent across more than two independent repeats. For comparisons between any two groups, Student's two-tailed t test was used, except for K where the Bonferroni-corrected adjusted P value was used. Source data are available for this figure: SourceData FS2.
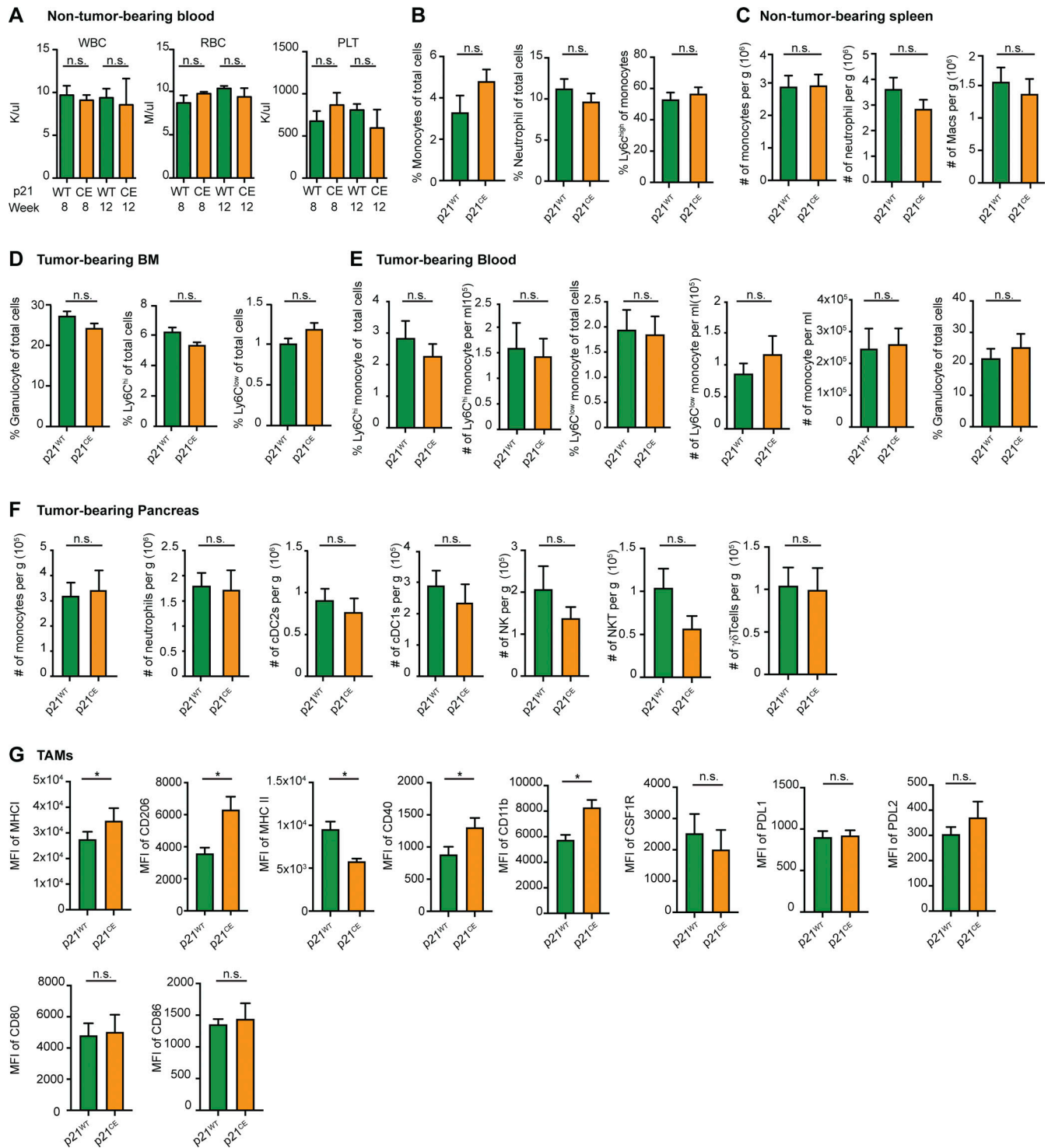
Figure S3. **Immune compositions in non-tumor- and tumor-bearing p21$^{CE}$ and p21$^{WT}$ mice. (A)** Quantification of white blood cells, red blood cells, and platelets in non-tumor-bearing p21$^{WT}$ and p21$^{CE}$ mice at weeks 8 and 12; $n$ = 3–4 mice/group. **(B)** Flow cytometry quantification of total monocytes, neutrophils, and Ly6Chi monocytes in blood of non-tumor-bearing p21$^{WT}$ and p21$^{CE}$ mice; $n$ = 7–9 mice/group. **(C)** Flow cytometry quantification of monocytes, neutrophils, and macrophages in the spleens of 8–12 wk p21$^{WT}$ and p21$^{CE}$ non-tumor-bearing mice; $n$ = 7–9 mice/group. **(D and E)** Flow cytometry quantification of myeloid cells in bone marrow and blood of tumor-bearing p21$^{CE}$ and p21$^{WT}$ mice; $n$ = 6 mice/group. **(F)** Flow cytometry analyses of the number of monocytes, neutrophils, cDC2s, cDC1s, NK cells, NKT cells, and γδT cells in the pancreas of p21$^{CE}$ and p21$^{WT}$ mice bearing orthotopic KP-2 tumors; $n$ = 6 mice/group. **(G)** Bar graphs showing the MFI of MHCI, CD206, MHCII, CD40, CD11b, CSF1R, PDL1, PDL2, CD80, CD86 in TAMs from p21$^{WT}$ and p21$^{CE}$ mice bearing orthotopic KP-2 tumors. Data were pooled from multiple independent experiments. $n$ = 6 mice/group. All graphs are expressed as the mean ± SEM. *, $P < 0.05$. For comparisons between any two groups, the Student's two-tailed $t$ test was used.
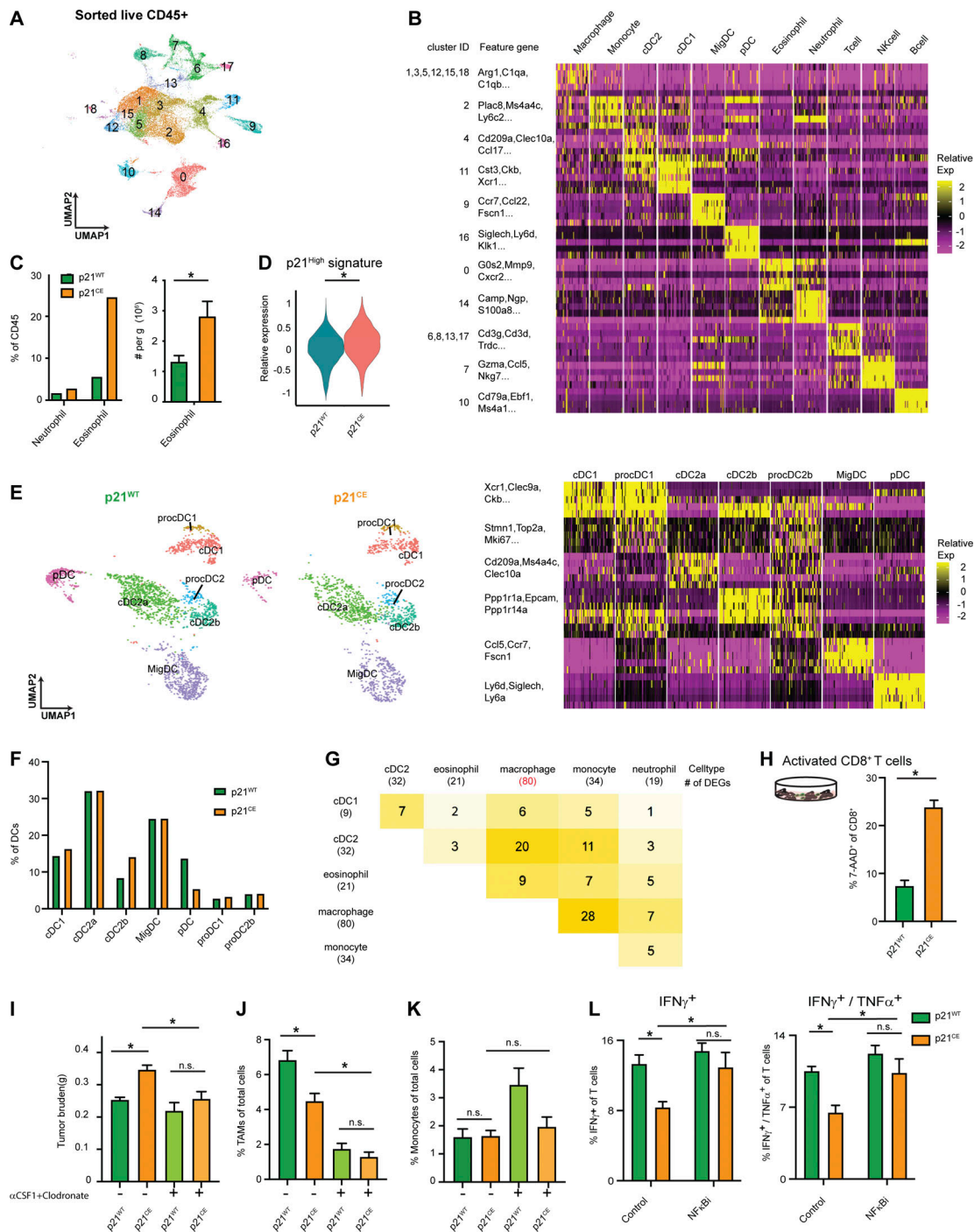
Figure S4. **scRNAseq analyses on tumor-bearing p21^CE and p21^WT mice and ex vivo T cell assays. (A)** UMAP plot of all sorted CD45+ cell clusters on merged objects from p21^CE and p21^WT KP-2 orthotopic tumor–bearing mice. Three mice were pooled for each genotype. **(B)** Heat map listing all clusters in A and corresponding cell type annotations and key gene expressions. **(C)** Bar plot displaying the percentages of neutrophils and eosinophils in p21^WT and p21^CE tumor-bearing mice from single cell analysis and number of eosinophils per gram of pancreas from flow cytometry analyses. **(D)** Violin plot displaying the expression levels of p21^High signature scores, identified in Fig. 4 M, in TAMs from p21^CE and p21^WT mice. *, Wilcox-adjusted P value < 0.05. **(E)** UMAP plot of the reclustered DC populations in Fig. 6 A, annotated with cell type and associated key gene expressions in the heat map (right). **(F)** Quantification of major DC populations identified in E from p21^CE tumors when compared with p21^WT tumors. **(G)** Heat map showing the number of shared DEGs between two genotypes in each cell population, including macrophage and close lineages. The number of DEGs for each single-cell population when comparing p21^CE to p21^WT was listed in the parenthesis below. **(H)** Bar plot displaying the percentage of 7-AAD+CD8+ T cells activated with CD3/CD28 Dynabeads (Gibco) when cocultured with BMDMs from p21^CE and p21^WT mice for 48 h. Data were consistent in three independent repeats. **(I–K)** Bar plot showing the tumor burden, percentages of TAMs and monocytes in p21^WT and p21^CE mice bearing orthotopic KP-2 tumors with or without CSF1 and clodronate treatment; n = 8–10 mice/group. **(L)** Bar plot displaying the mean percentage of IFNγ+ and IFNγ+TNF-α+ CD8 T cells in culture with BMDMs from p21^CE and p21^WT mice for 5 h with or without pre-exposure to NF-κB inhibitor. *, P < 0.05. For comparisons between any two groups, the Student's two-tailed t test was used. All in vitro assays are representative of two to three agreeing independent repeats.
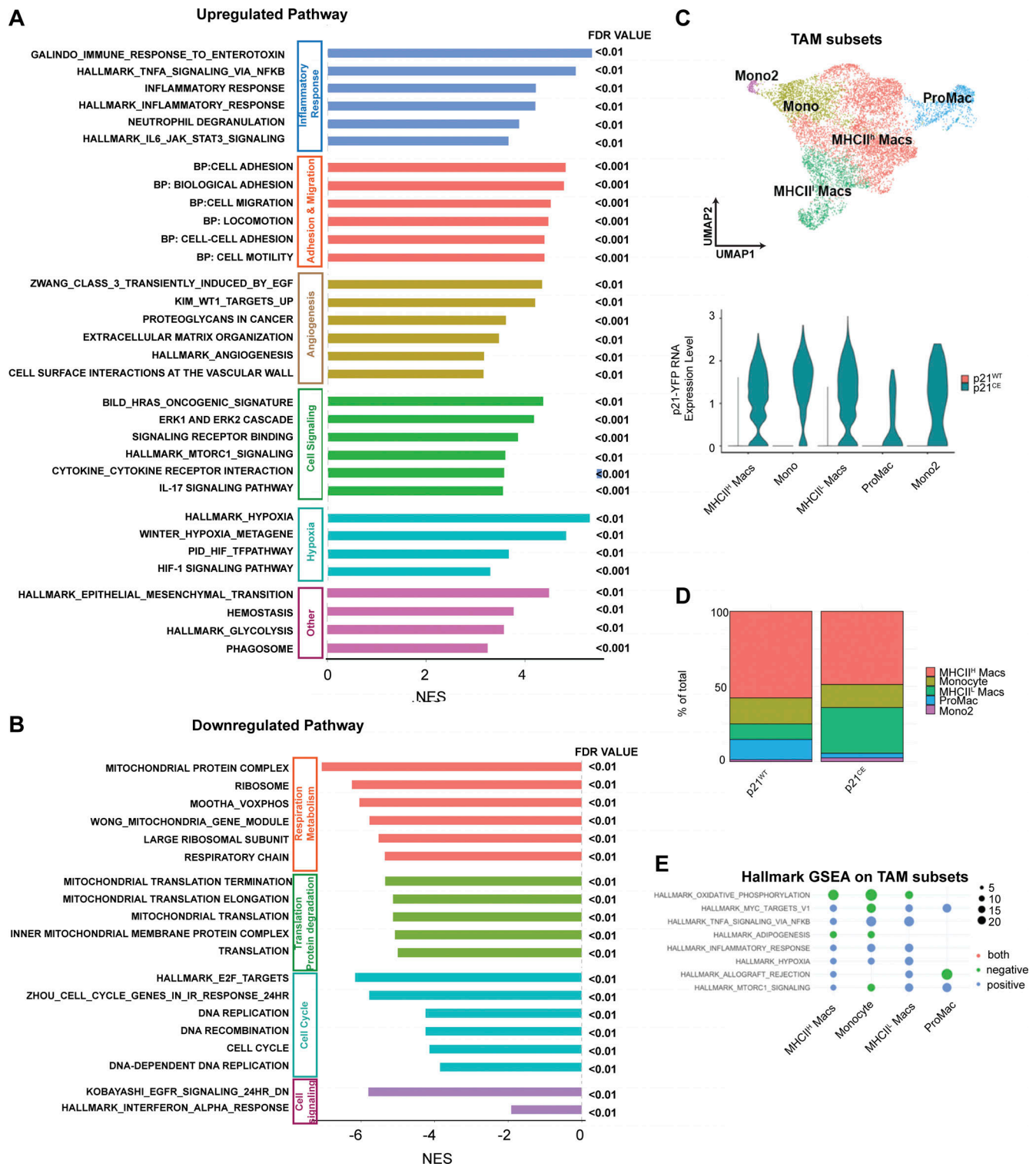
Figure S5. **GSEA analyses of comparing p21$^{CE}$ and p21$^{WT}$ TAMs. (A and B)** Bar plot showing significantly upregulated and downregulated pathways identified by GSEA in TAMs from p21$^{CE}$ compared with p21$^{WT}$ mice. The pathways were grouped into biological functions with FDR <0.01. **(C)** UMAP of reclustered macrophage and monocyte clusters from Fig. 6 C and annotated with major subpopulations. Violin plot showing the expression of p21-YFP construct in each cluster. **(D)** Bar plot showing the composition of each subpopulation as of total macrophages/monocytes from p21$^{CE}$ and p21$^{WT}$ mice. **(E)** Dot plot showing the result from GSEA when comparing each cluster of cells from p21$^{CE}$ to p21$^{WT}$ counterpart; dot size represents gene ratio, and color represents either positive or negative enrichment.

Provided online are Table S1 and Table S2. Table S1 shows the array of top regulated genes (sip21 vs. siNT; *n* = 3 each). Table S2 lists key resources.